Effect of Active Carbonyl-Carboxyl Ratio on Dynamic Schiff Base Crosslinking and Its Modulation of High-Performance Oxidized Starch-Chitosan Hydrogel by Hot Extrusion 3D Printing

Junchao Zhu [a], Fengwei Xie [b], Zhipeng Qiu [a, *], Ling Chen [a, **].

[a] *Ministry of Education Engineering Research Center of Starch & Protein Processing, Guangdong Province Key Laboratory for Green Processing of Natural Products and Product Safety, School of Food Science and Engineering, South China University of Technology, Guangzhou 510640, China*.

[b] *School of Engineering, Newcastle University, Newcastle Upon Tyne, NE1 7RU, United Kingdom*

[*] Corresponding author. Email: fesolorway@mail.scut.edu.cn (Z. Qiu)

[**] Corresponding author. Email: felchen@scut.edu.cn (L. Chen)

Abbreviations

MS, maize starch; OS, oxidized starch; ACR, active carbonyl-carboxyl ratios; CS, chitosan; OSC, oxidized starch and chitosan; POSC, printed oxidized starch and chitosan. *CI*, crosslinking index; DSR, dynamic shear rheology; τ_y, yield stress point; τ_f, flow stress.

ABSTRACT

The quest to develop 3D starch-based printing hydrogels for the controlled release of active substances with excellent mechanical and printing properties has gained significant attention. This work introduced a facile method based on crosslinking via Schiff base reaction for preparing bicomponent hydrogels. The method involved the utilization of customizable oxidized starch (OS) and chitosan (CS), enabling superior printing performance through the precise control of various active carbonyl -carboxyl ratios (ACR, 2:1, 1:1, and 2:3, respectively) of OS. OS-CS hydrogel (OSC) with an ACR level of 2:1 (OS-2-*y*%CS) underwent rearrangement during printing environment, fostering increased Schiff base reaction with a higher crosslinking degree and robust high structural recovery (>95%). However, with decreasing ACR ratio (from 2:1 to 2:3), the printing performance and mechanical strength of printed OSC (POSC) declined due to lower Schiff base bonds and increased phase separation. Compared with printed OS, POS-2-2%CS exhibited a remarkable 1250.52% increase in tensile strength and a substantial 2424.71% boost in compressive strength, enhanced shape fidelity and notable self-healing properties. Moreover, POS-2-2%CS exhibited stable diffusive drug release, showing potential application in the pH-responsive release of active substances. Overall, controlling the active carbonyl-carboxyl ratios provided an efficient and manageable approach for preparing high-performance 3D-printed hydrogels.

Keywords: Starch hydrogels; hot extrusion 3D printing; carbonyl/carboxyl ratios; Schiff base bonds; mechanical properties.

1. Introduction

Hydrogels, a versatile soft material, find widespread application in tissue scaffolds, flexible devices, and targeted delivery (Hafeez et al., 2023; Soleymani Eil Bakhtiari et al., 2021). Currently, hot extrusion 3D printing emerges as an environmentally friendly technology for straightforward manufacturing (Li, Wu, Chu, & Gelinsky, 2020). This technique, rooted in computer numerical modeling, constructs hydrogel materials by layering polymer materials, offering advantages like continuous production and eco-friendliness (Li, Tan, Leong, & Li, 2017; Narupai, Smith, & Nelson, 2021). Meanwhile, the hydrothermal effect of the 3D printing process, coupled with the shear force exerted by extrusion machinery, induces interactions such as entanglement, physical crosslinking, and hydrogen bonds between molecular chains. As a result, a porous agarose network structure is created that could be adjusted to meet the needs of creating novel controlled-release materials (Li et al., 2017).

Starch is a natural compound consisting of hydroxyl-rich glucose units that facilitate intermolecular crosslinking via hydrogen bonds to form hydrogel networks. However, the inherent limitations of monocomponent starch inks, such as poor mechanical properties and printability (Zhang et al., 2018), pose challenges like extrusion into drops, uneven extrusion, and inadequate self-supporting ability. These issues make it difficult to maintain the original ink performance (Lee, Gillispie, Prim, & Lee, 2020; Seoane-Viaño, Januskaite, Alvarez-Lorenzo, Basit, & Goyanes, 2021). In our previous studies, we developed a hot extrusion 3D printing method for oxidized starch (OS) hydrogels with excellent hydration (Qiu, Zheng, Xu, Chen, & Chen, 2022). Additional advancements included the development of microporous starch hydrogels through the controlled release of Ca^{2+} for

wound hemostasis (Zheng et al., 2023). Recent studies have explored improving the structure of 3D printed inks via crosslinking agents (Mea, Delgadillo, & Wan, 2020), light curing (Ahn, Stevens, Zhou, & Page, 2020; Khalfa, Becker, & Dove, 2021), and support bath assistance (Kang et al., 2021) to achieve controlled release. Some researchers have enhanced mechanical properties by introducing biomolecules with amino groups (Wu et al., 2020), hydroxyl groups (Lu et al., 2020), active carbonyl groups (Zhao et al., 2022), and carboxyl groups (Zhang et al., 2018) as a crosslinking agent to form a new crosslinking network. However, adapting these modified starch hydrogels to the dynamic mechanical changes at different stages in the 3D printing environment remains challenging, hindering the formation of high-performance hydrogels. Besides, the incorporation of multiple cross-linkers increases viscosity, leading to extrusion difficulties. Therefore, there is a need for continued exploration in the fabrication of starch inks with dynamic covalent/non-covalent combinations through hot extrusion 3D printing.

Chitosan (CS) arises from partial acyl group removal from chitin (Balaji, Pakalapati, Khalid, Walvekar, & Siddiqui, 2018; Zhao, Guo, Wu, Liang, & Ma, 2018). As an alkaline polysaccharide with amino groups, CS has attracted considerable attention in the biomedical and food fields due to its favorable biocompatibility and bacteriostatic properties (Kácerová et al., 2024; Li et al., 2020; Taghizadeh et al., 2022). It has been reported that OS-CS (OSC) hydrogels, prepared by dynamic Schiff base bonds between the active carbonyl groups in OS and the amino groups in CS, exhibit excellent properties for rapid gelation (Serrero et al., 2010). In the presence of OS, the amino groups in CS not only engage in Schiff base with active carbonyl groups (aldehyde and ketone groups) in OS but also interact with its carboxyl groups by electrostatic force (Farooq, Ahmad, Zhang,

& Zhang, 2023; Li et al., 2017). This dual interaction influences the crosslinking in the composite hydrogels and their properties (such as release in different pH) (Guo, Liang, & Dong, 2023; Zhao et al., 2020). From a cross-linked hydrogels design standpoint, controlling the active carbonyl-carboxyl ratios (ACR) of OS emerges as a convenient strategy to modulate the crosslinking form, thereby influencing the properties of hot extrusion 3D printed starch hydrogels. However, the effect of ACR level on dynamic covalent crosslinking and the modulation mechanism on OSC hydrogels through hot-extruded 3D printing requires further elucidation.

In this study, various levels of ACR in OS, with a similar total content of active carbonyl and carboxyl groups, were first prepared and then mixed with different amounts of CS to formulate OSC inks. Then, the studies commenced using a rheometer to simulate the changes in viscosity, shear-thinning characteristics, and thixotropy of different OSC during the 3D printing process. This aimed to elucidate the relationship between the printing properties of hydrogels and the ACR level, as well as the amounts of CS. Moreover, their effect on the mechanical strength, hydration ability, and self-healing capability of hydrogels were extensively examined. Finally, a catechin release model was constructed to analyze the pH-responsive release behavior of the hydrogels. Overall, this study offers a fresh perspective on designing high-strength 3D-printed starch hydrogels with tunable physical and functional properties.

2. Experimental section

2.1 Materials

Maize starch (MS, molecular weight (M_w) of 2.17×10^7 g/mol and amylose content of 21.46%) was purchased from Qinhuangdao Pengyuan Starch Co., Ltd (Shandong, China).

CS (degree of deacetylation over 95% and M_w of 150 kDa according to the supplier), NaClO, $NH_2OH \cdot HCl$, HCl, NaOH, $AgNO_3$, ninhydrin, and catechin (purity ≥ 98%) were purchased from Sigma Chemical Co. (St. Louis, USA). All chemical reagents are analytically pure reagents.

2.2 Preparation and measurement of MS/OS

2.2.1 Preparation of OS

OS with varying ACR levels but similar active carbonyl + carboxyl contents were synthesized using the NaClO system. NaClO is a non-specific oxidizing agent that oxidizes the hydroxyl group of starch first to active carbonyl groups (aldehyde and ketone groups) and then further oxidizes it to carboxyl groups (Chatterjee, Pong, & Sen, 2015; Haq et al., 2019). Notably, pH has a significant effect on NaClO. Under acidic conditions, NaClO takes the form of HClO and Cl_2, which prefer to oxidize the hydroxyl group to an active carbonyl group rather than to a carboxyl group (Chen et al., 2015b; Cheng et al., 2022; RUTENBERG & SOLAREK, 1984; Tolvanen, Mäki-Arvela, Sorokin, Salmi, & Murzin, 2009).

A suspension with a 30% mass concentration of MS was prepared, stirred, and reacted with 6% effective chlorine addition for 2 h at a specific temperature and pH under closed conditions. NaClO was consistently added in a continuous-flow manner. The pH range of 5–9 was selected due to the potential for hydrolysis and instability in reaction environments with a pH below 5 or above 10 (Chen et al., 2015a). To maintain pH stability, 0.10% NaOH was introduced during oxidation. From our preparation, OS with an ACR of 2 was prepared at 12 ℃ and pH 5 and noted as OS-2. OS with ACR of 1 or 0.67 were prepared at pH 7 or pH 9 and 15 ℃ were recorded as OS-1 and OS-0.67, respectively. Then, OS underwent

multiple washing, centrifugation, and filtration steps. Subsequently, it was transferred to an oven at 45 ℃ for 12 h–15 h until the moisture content was reduced to 13.00%–14.00%. Finally, the dried samples were ground and sieved through an 80-mesh screen for subsequent testing.

2.2.2 Structural and properties characterization

To determine the active carbonyl group contents, HCl titration was performed, where active carbonyl groups react with hydroxylamine hydrochloride to form an oxime and HCl (Bryant & Smith, 1935). Then, the carboxyl group content was determined using acid-base titration (Dence, 1992). Specifically, 30.00 mg of MS/OS and 0.5 mL dimethyl sulfoxide-d6 were placed into a 5 mL stoppering tube and oscillated at 90 ℃ for 1 h for the nuclear magnetic resonance (NMR) test. ^{1}H-NMR and ^{13}C-NMR were determined by a 600 M superconducting NMR spectrometer (NMR, Bruker, AVABNCE III HD600, Germany) with 64 times and 4096 times, respectively (Qiu, Zeng, Xu, Zheng, & Chen, 2023). The chemical groups of MS/OS were determined by Fourier-transform infrared spectroscopy (FTIR) using attenuated total reflectance spectroscopy (Bruker, NICOLET IS50, Germany) (Ahn et al., 2020). The M_w of the MS/OS was determined using a GPC system coupled with a MALS detector (632.80 nm, DAWN HELEOS, Wyatt Technology, Santa Barbara, CA, USA) and a refractive index detector (Optilab rex, Wyatt Technology), as detailed in our earlier publication (Qiu et al., 2023). The thermal viscosity, crystalline structure, and thermal stability of MS/OS were measured by Brabender viscometer (Moorthy, 1985), X-ray diffraction (XRD, PANalytical B.V., X-pert PRO, Netherlands) (Qin et al., 2019) and differential scanning calorimetry (DSC, PerkinElmer, Diamond-I, USA) (Khalfa et al., 2021), respectively. Subsequently, the granular surface structure and solubility of MS/OS

were determined by a polarizing microscope (Zeiss, Axioskop 40, Germany) (Pérez, Baldwin, & Gallant, 2009) and the related methods (Mandala & Bayas, 2004). Finally, the nanoparticle size and zeta potential of MS/OS were measured using a Malvern Nano-ZS ZEN3600 instrument (Malvern, Malvern PANalytical, UK) equipped with a 4 mW helium/neon laser at a wavelength output of 633 nm and a backscattering angle of 173° at pH 7 and 25 ℃ (Huang, Li, Chen, & Li, 2017). See Supporting Information (SI) for additional details on the oxidation process and further tests.

2.3 Preparation and measurement of OS/OSC inks

2.3.1 Preparation of OS/OSC inks

Initially, CS (2.00 g) was mixed with 98.00 mL phosphate-buffered saline (PBS, pH 5) and stirred at 300 rpm for 12 h to ensure dissolution. To prepare OSC inks, 10.00 g of OS and CS solution were mixed and then stirred at 72 ℃, 100 rpm for 30 min. See **Figure 1a** for ink preparation. OS-*x*-*y*%CS designates OSC with an ACR level of *x* and a CS addition of *y*.

2.3.2 Crosslinking degree measurement

First, 2.00 mg of OSC flours and 1.00 mL of deionized water were mixed in a 10 mL centrifuge tube, thoroughly stirred, and allowed to rehydrate at room temperature for 12 h. Then, 1.00 mL of 2% ninhydrin was added and then left at 100 ℃ for 20 min, followed by cooling to room temperature (Cui, Wu, Ni, Sun, & Cheng, 2022). The absorbance value was measured at 570 nm using an Evolution 201 UV-visible spectrophotometer (Thermo Scientific, USA). The crosslinking index (*CI*) was calculated using the formula (Eq. 1).

$$CI\ (\%) = (1 - B_1 / B_0) \times 100\% \quad \text{(Eq. 1)}$$

where B_1 is the absorbance value of OSC/POSC, and B_0 is the absorbance value at

equimolar amounts of the active carbonyl + carboxyl in OSC.

2.3.3 Rheological measurement

OS/OSC inks (3.00 g) were placed on the rheometer plate (70 ℃) for rheological assessments. After allowing the samples to equilibrate for 5 min, testing was conducted using a 25 mm parallel plate rheometer (Anton Paar, MCR302, Austria) (Zheng et al., 2023). In the dynamic frequency sweep, the strain and angular frequency were set at 1% and 1 to 100 rad/s (Nishiguchi & Taguchi, 2020). The steady shear involved a shear range of 10^{-1} to 10^{2} s^{-1}, with low and high shear rates set at 1% and 100%, respectively. The strain sweep encompassed a 0.1 to 100% range at 10 rad/s (Hafeez et al., 2023).

2.4 Printing of OS/OSC (POS/POSC) hydrogels

OS/OSC inks were loaded into the 70 ℃ print barrel and left for 5 min (SHINNOVE S2 HE-3D printer, China) (Qiu et al., 2022). The printing parameters were set as follows: nozzle height of 1.00 mm, nozzle diameter of 0.80 mm, printing speed of 50 mm/s, retraction speed of 40 mm/s, and retraction distance of 4.5 mm. The self-supporting layer of a hollow cylinder and the printed fidelity of triangles (After printing, after 1 h, and after 24 h) were recorded (Lee et al., 2020). Then, the POS/POSC hydrogels were frozen at -80 ℃, subjected to vacuuming, dried at -40 ℃, and then sieved through an 80-mesh screen. POS-*x*-*y*%CS designates POSC with an ACR of *x* and a CS addition of *y*.

2.5 Structural and properties measurements of POS/POSC hydrogels

2.5.1 Structural measurement

Structural characterization methods were mainly drawn from previous studies (Ahn et al., 2020; Cui et al., 2022; Li et al., 2017; Qin et al., 2019; Serrero et al., 2010). The *CI* of OSC flours after printing and after 1 h of printing was determined according to

Experimental section 2.3.2. The chemical bonds and crystalline structure of CS/POS/POSC flours were measured by FTIR and XRD according to Experimental section 2.2.2, respectively. The microstructure of lyophilized POSC hydrogels after printing, after 24 h of placement, and after swelling was observed via scanning electron microscopy (SEM, Zeiss, Merlin EVO18, Germany) at 20 kV and 200X/500X magnification. See SI for additional details.

2.5.2 Mechanical properties measurement

The tensile force (g) and distance (mm) of POS/POSC hydrogels after printing, after 1 h, and after 24 h were assessed using the HDP/PFS probe of a TA-XT Plus texture analyzer (SMS, UK) in tensile mode (Zheng et al., 2023). The compressive strain was measured employing the P36R probe in compression mode. The pre-test speed, test speed, and trigger force were 2 mm/s, 1 mm/s, and 5 g, respectively (Lu et al., 2020).

2.5.3 Water distribution measurement

Water distribution of POS/POSC hydrogels was examined using low-field NMR (Niumag, NMI20-040H-I, China) (Qiu et al., 2022). The main frequency and spectral width were set at 20.00 kHz and 817.62 kHz, respectively. Sampling points and their repetition times were 800018 and 10000 ms, respectively.

2.5.4 Thermal stability measurement

The thermal stability of POS/POSC hydrogels was determined concerning Experimental section 2.2.2. Thermogravimetry, derivative thermogravimetry, and DSC of lyophilized POS/POSC hydrogels were analyzed through a Synchronous thermal analyzer (STA449F3, NETZSCH Company, Germany) with the temperature of 30 ℃ to 260 ℃ at 20 ℃ /min in a nitrogen atmosphere.

2.5.5 Hydration measurement

For the water retention test, POS/PSOC hydrogels saturated with 10.00 mL of deionized water were placed at 37 ℃ for 7 h, and the hourly weight changes were recorded (Kang et al., 2021; Qiu et al., 2022). Then, the water-lost hydrogel was soaked in PBS at pH 7.4 and 37 ℃ for 168 h to test the swelling rate (Zheng et al., 2023) (Eq. 2).

$$Swelling\ ratio\ (\%) = (W_t - W_0) / W_0 \times 100\% \quad \text{(Eq. 2)}$$

where W_t and W_0 denote the weights of hydrogels after swelling at each time point and initial weight, respectively.

Then, the microstructure of POS/POSC hydrogels after swelling and swelling for 7 d were analyzed by Environmental SEM (Quanta 200 ESEM, FEI, Netherlands) at 20.0 kV and 500X/1kX, respectively (Bao et al., 2019).

2.5.6 Self-healing measurement

In the self-healing assessment, POSC hydrogels were dyed with a blue pigment and allowed to stand for 0.5 h and 24 h. The changes in the contact surface were then observed (Hafeez et al., 2023).

2.5.7 The pH response measurement

According to Experimental sections 2.3 and 2.4, OSC solution dissolved with 10.00 mg of catechin was used for 3D printing of POSC hydrogels. POSC hydrogels, loaded with 10.00 mg of catechin were immersed in 50 mL of pH 5.0/7.4 PBS at the thermostat water bath (37 ℃) and mild shaking (170 rpm). Then, 1.00 mL of the reaction solution was pipetted with simultaneous rehydration treatment and measured at 280 nm (Qin et al., 2019) at the following time points: 0 h, 0.2 h, 0.4 h, 0.6 h, 0.8 h, 1 h, 2 h, 3 h, 4 h, 5 h, 6 h, 12 h, 24 h, 72 h, and 168 h. In addition, the absorbance values of different concentrations of

250 catechins (0.00 mg/mL, 0.02 mg/mL, 0.04 mg/mL, 0.06 mg/mL, 0.08 mg/mL, and 0.10
251 mg/mL) at 280 nm were determined for plotting the calibration curve. The cumulative
252 release percentage was calculated with the formula below (Eq. 3) (Cui et al., 2022). The
253 cumulative release was graphed as the percent cumulative release of catechins versus time.

254 $$Cumulative\ release\ percentage\ (\%) = (V_e \sum_{i=1}^{n-1} C_i + V_0 C_n) / W_0 \times 100\% \quad \text{(Eq. 3)}$$

255 where V_e is the volume of PBS rehydration (1.00 mL), C_i/C_n is the release concentration at
256 the time point t (mg/mL), V_0 means the initial volume of PBS (50.00 mL), W_0 is the mass
257 of loaded catechin (10.00 mg).

258 Furthermore, the release kinetic and release mechanism of catechin from POSC
259 hydrogels was performed by fitting the experimental data using the models (zero order,
260 first order, Hixson-Crowell, Higuchi, and Korsmeyer-Peppas) (Varma & Kumar, 2017).

261 **2.6 Statistical analysis**

262 Data were analyzed with IBM SPSS 26 (New York, USA), expressed as mean ±
263 standard deviation, and statistically compared using Duncan's one-way analysis of
264 variance ($p \leq 0.05$).

265 **3. Results and discussion**

266 **3.1 Characterization of MS/OS**

267 Three OS samples with varying ACR levels (2, 1, and 0.67, respectively) but similar
268 active carbonyl + carboxyl contents (nearly 2.5%) were synthesized using NaClO (**Figure**
269 **1a**, **Figure 2a** and **Table S1**) ($p < 0.05$). As shown in **Figure 2b**, comparing MS, the
270 hydrogen proton cleavage of OS at 5.40 pm to 5.60 ppm was evident, suggesting an impact
271 on the -OH group at the C2,3 position. Additionally, a hydrogen proton peak at 8.20 ppm
272 in OS, corresponding to the presence of aldehyde groups, gradually disappeared as the

ACR level increased. In ^{13}C-NMR results (**Figure 2c**), it was observed that OS exhibited a new distinctive peak at 90.00 ppm, which may be attributed to the formation of hemiacetals. The hydroxyl groups of C2 and C3 were oxidized to ketone groups, which can react with water to form hemiacetals (Yi, Zhang, & Ju, 2014). As the degree of oxidation increased (ACR level decreased), the C6 primary hydroxyl signal of OS at 63.40 ppm gradually weakened. There was a faint peak at 195.60 ppm in OS-2, corresponding to the C6 aldehyde group signal gradually, which disappeared as the ACR level increased (Kato, Matsuo, & Isogai, 2003). Meanwhile, the C6 carboxyl group signal of OS at 178.60 ppm gradually enhanced with an increase in the oxidation degree and reached a maximum at OS-0.67 (Kato et al., 2003). FTIR results (**Figure 2d**) indicated that compared to MS, there was a new stretching vibration peak in the OS. Specifically, the carbonyl (OS-2) and carboxyl (OS-1, OS-0.67) stretching vibration peaks appeared at 1733 cm^{-1} and 1600 cm^{-1}, respectively, indicating that successful oxidation of hydroxyl groups on the glucose unit to the carbonyl groups, and further to carboxyl groups (Chen et al., 2015a; Kizil, Irudayaraj, & Seetharaman, 2002).

Considering that the oxidation reaction based on NaClO not only destroyed the starch glucose units but also broke the starch molecular chains and thus may affect the properties of starch hydrogels (Shokri et al., 2022). Therefore, the M_w and the thermal viscosities of MS and OS were determined. As shown in **Table S1**, compared to MS ($M_w = 2.17\times10^7$ g/mol), M_w decreased from 0.916×10^6 g/mol to 0.857×10^6 g/mol for OS-2 and OS-0.67, respectively. The thermal viscosity results (**Figure 2e** and **Table S1**) also showed no significant difference in values of peak viscosities among different OS. These phenomena indicated that parts of the starch molecular chains were broken during the oxidation process,

which led to the reduction of amylopectin clusters and the reduction of amylose chain lengths, which in turn led to the reduction of the viscosity of the starch molecules during the pasting process. This suggested that the various oxidation levels did not significantly alter the structures of MS, which was further confirmed by XRD, DSC, and polarizing microscopy analyses (**Figure S1a–S1b** and **Figure S2**).

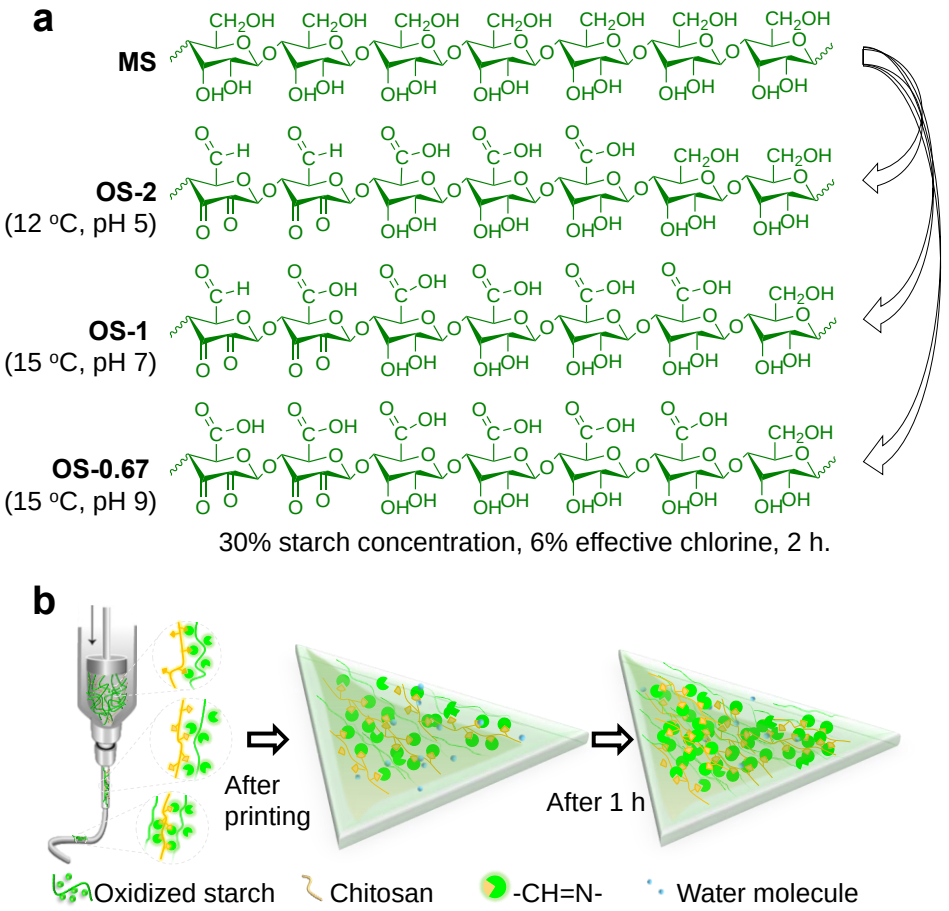

Figure 1. Schematic diagram of chemical functionalization (a) and 3D printing process (b).

Then, the solubility, size, and zeta-potential (**Figure 2f** and **Figure S1c**) of OS exhibited a noteworthy change compared to MS, which was further enhanced with an increasing degree of oxidation. This could be attributed to the increased hydrophilicity and anionic content resulting from the rise in carboxyl contents (Qiu et al., 2023; Wu & Lai,

2019). Interestingly, the nano sizes of OS (y = 2 (0.13 μm), 1 (0.12 μm), and 0.67 (0.12 μm)) were reduced compared to MS (0.15 μm), with no significant differences observed within different OS ($p \leq 0.05$). This might be related to the increased negative charge value, as the electrostatic repulsions between the OS made it difficult to aggregate, ultimately leading to a smaller average particle size than MS. In short, three OS samples with different ACR levels but similar structures were successfully prepared.

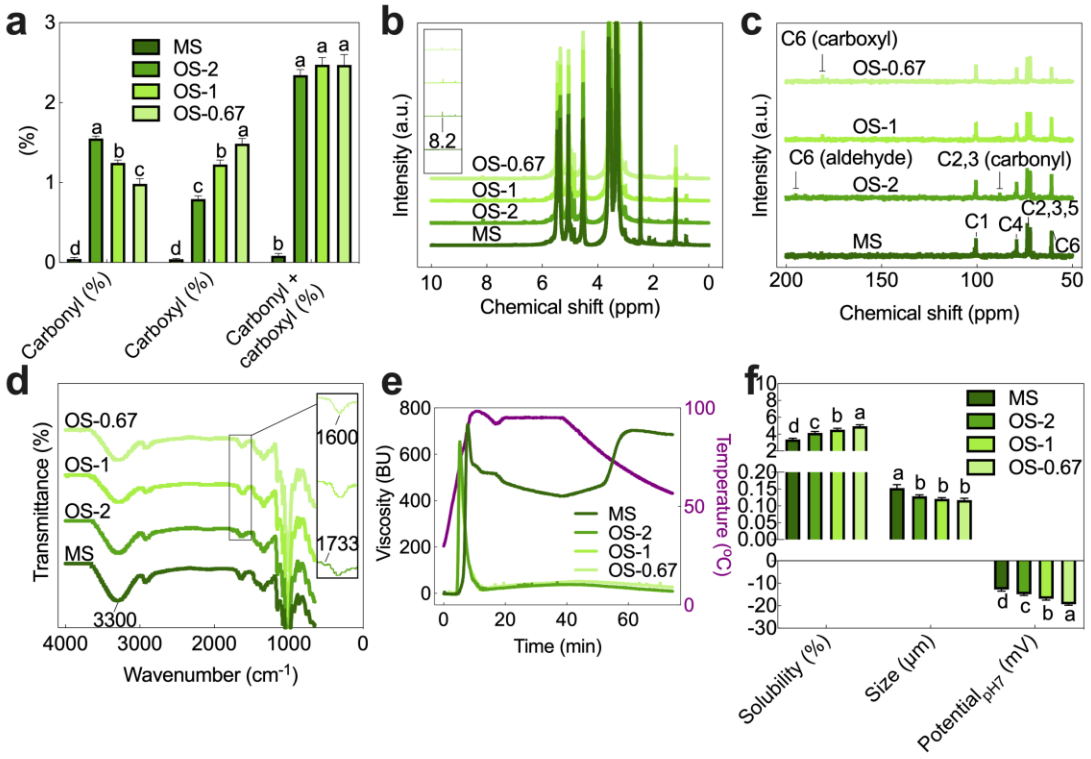

Figure 2. ACR (a), ^{1}H-NMR curves (b), ^{13}C-NMR curves (c), infrared spectra (d), thermal viscosity profile (e), solubility, nanoparticle size, and potential (f) of MS/OS.

3.2 Crosslinking degrees of OSC inks

In OSC inks, the amino groups within CS could participate in crosslinking via Schiff base and electrostatic interactions with active carbonyl and carboxyl groups in OS, respectively. These interactions significantly influenced the overall properties of the ink.

The pH across all OSC inks fell within the range between 6.33 and 6.45, highlighting the stability of the Schiff base reaction and electrostatic interactions since Schiff bases would decompose and electrostatic interactions would vary in an acidic environment (**Figure S3a** and **Table S2**) (Antony, Arun, & Manickam, 2019; Jia & Li, 2015; Lee et al., 2020). Then, the content of free amino groups in OSC was determined to confirm the crosslinking degrees. The *CI* (**Figure 3a**) exhibited a steady increase with the elevation of both ACR levels and the amount of CS. For example, OS-2-2%CS demonstrated a substantial 63.90% increase in *CI* compared to OS-0.67-2%CS, suggesting a heightened occurrence of Schiff base reaction (Li et al., 2020).

3.3 Rheology of OS/OSC inks

In the 3D printing environment, the inks undergo distinct phases, including holding, extrusion, and self-supporting phase, which require (i) shear-thinning capability, (ii) suitable viscoelasticity and flow stress for extrusion from the nozzle, and (iii) certain yield stress for non-collapse (Lee et al., 2020; Li et al., 2017; Li et al., 2020). To gain deeper insights into ink properties, their rheological characteristics were evaluated. All inks demonstrated shear-thinning behavior, evident in the viscosity-shear rate curves (**Figure 3b**). According to the Power-law rheological model (Hafeez et al., 2023), the inks exhibited flow characterization index (n) values below 1 **(Figure S3b** and **Table S2)**, classifying them as typical non-Newtonian fluids. Dynamic frequency testing (**Figure 3c–3d**) revealed that the storage modulus (G') consistently exceeded the loss modulus (G'') for all the ink formulations, indicating the presence of a viscoelastic network. Compared with the original oxidized sample (OS), G', G'', and zero-shear-rate viscosity of the OSC showed an increase when the ACR level was decreased. The peak values were achieved at OS-0.67-2%CS,

which can be attributed to both physical entanglement induced by CS and crosslinking, particularly through electrostatic interactions (Wu et al., 2020). OS-2-*y*%CS, particularly OS-2-2%CS, exhibited greater susceptibility to structural damage under shearing due to potential damage to the crosslinking points in the dynamic crosslinked network, primarily based on the Schiff base reaction when the addition of CS was increased or the ACR level was decreased.

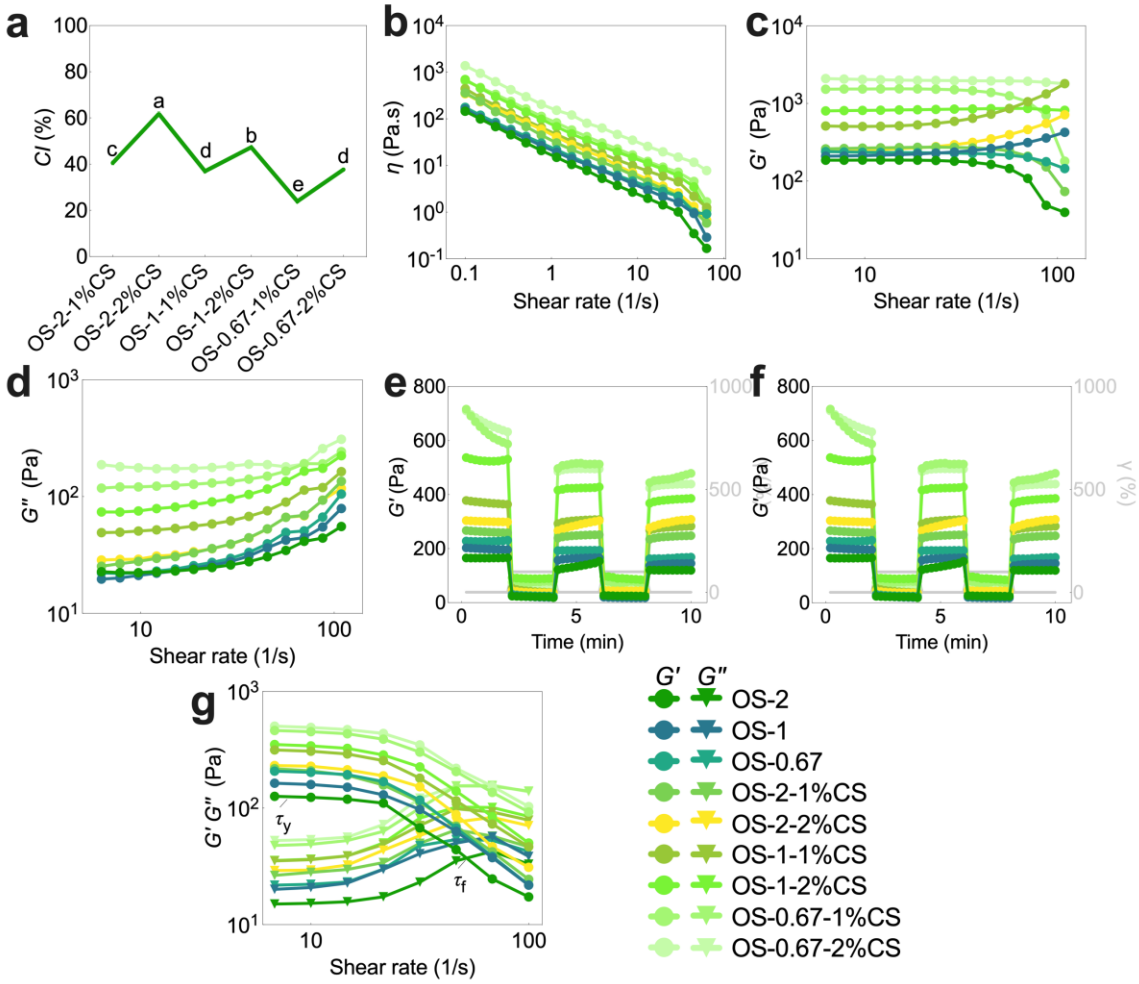

Figure 3. *CI* (a), stabilizing shear (b), dynamic frequency (c, d), thixotropy (e, f), and strain shear (g) of OS/OSC inks.

Dynamic shear rheology parameters, $DSR_{3\text{-}1}$ and $DSR_{5\text{-}3}$, were used to evaluate the thixotropic behavior of the gel materials (**Figure 3e–3f**, **Figure S4a–S4b**, and **Table S2–**

S4). The DSR values ($G'_{3/1}$, $G'_{5/3}$, $G''_{3/1}$, and $G''_{5/3}$) of OSC exhibited a decreasing trend with the reduction of ACR, surpassing those of OS. At an ACR level of 2 and a CS addition of 2% (OSC-2-2%CS), the DSR values reached a peak (nearly 100%), indicating a higher rate of structural recovery (**Figure 4**). This dynamic crosslinked network demonstrated rapid recovery to its initial elasticity upon shear stress removal, facilitated by the presence of Schiff base bonds in a dynamic equilibrium (Nishiguchi & Taguchi, 2020; Zhao et al., 2022). As the shear rate continued to increase until reaching the yield stress point (τ_y), the mechanical strength of the hydrogel materials can be characterized. The τ_y (**Figure 3g**, **Figure S4c**, and **Table S5**) of OSC was larger than OS and significantly increased with a decrease in ACR level ($p < 0.05$), a result of interactions between CS and OS. Overall, the combination of strong shear-thinning behavior and high thixotropy exhibited by OS-2-*y*%CS, especially OS-2-2%CS, with increasing CS addition, made it an ideal candidate for 3D printing (Hafeez et al., 2023). The flow stress (τ_f) represents the stress value when G' equals G'' during the stress scanning process, serving as an indicator of material extrusion difficulty in the 3D printing process. Under shear, the Schiff base bonds were more readily broken and reorganized, reducing the flow stress of molecular chains and improving extrudability. Therefore, the minimum τ_f of OSC was observed at OS-2-*y*%CS and subsequently increased as the ACR decreased. With a decrease in active carbonyl group contents, the crosslinking effect of Schiff bases weakened, and intermolecular electrostatic interactions intensified, leading to an increase in flow stress. These effects became more pronounced with the increase of CS addition.

The macro-mechanical characteristics of inks were further evaluated (**Figure S4d**). All OS inks exhibited poor mechanical characteristics. Among OSC formulations, OSC-2-

y%CS with a high ACR level demonstrated superior structural recovery compared to other OSC variants, indicating satisfactory ductility. Additionally, OSC-2-*y*%CS displayed stability on the fork and remained adherent, suggesting higher interfacial bonds ability. In contrast, other OSC samples, specifically those with a value of $x = 0.67$, were observed to flow downward from the crevices of the fork and the surface of the spoon, respectively. Therefore, the addition of CS enhanced the intermolecular interactions, consequently enhancing both the shear-thinning behavior and structural recovery of OSC. This enhancement showed a strong positive correlation with the active carbonyl group contents and the CS amounts. These results were consistent with the thixotropic findings discussed above.

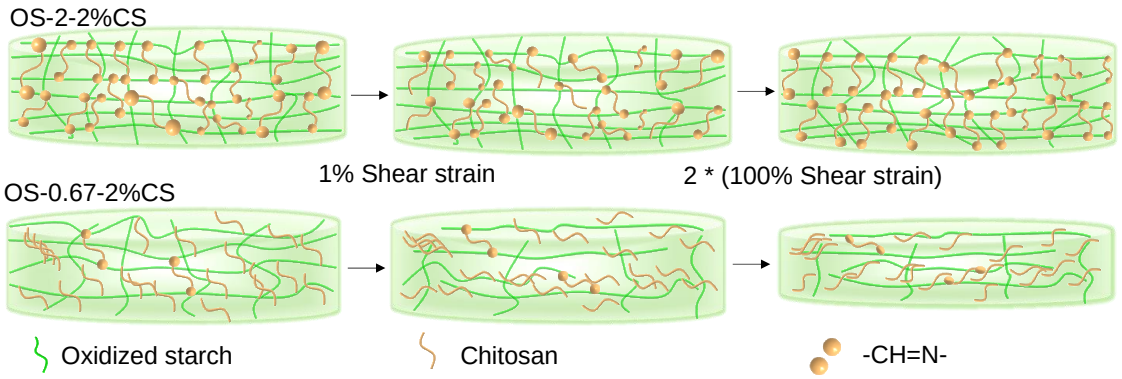

Figure 4. Schematic diagram of starch molecular chain movement during thixotropy.

3.4 Printing performance of POS/POSC hydrogels

Achieving printability and preserving shape fidelity are pivotal aspects in the 3D printing of hydrogels (Lee et al., 2020; Li et al., 2020). As shown in **Figure 5a–5b**, the shape fidelity of POS was found to be inferior, failing to maintain the original 3D model structure. It was reported that single polysaccharide hydrogels, such as alginate hydrogels (Li et al., 2017), showed weak mechanical properties, making it challenging to retain the entire 3D printed shape. This weakness resulted from the poor thixotropy of pure

polysaccharide hydrogels with single physical crossing (Schwab et al., 2020). Compared to POS, POSC showed superior shape fidelity, particularly in terms of the surface gloss of POS-2-*y*%CS (**Figure 5c**). Within the high-shear environment of nozzle extrusion, the molecular chains of OS and CS in POS-2-*y*%CS established the initial crosslinking network through intermolecular physical interactions (Schwab et al., 2020). Meanwhile, the formation of broken and reorganized Schiff base bonds established a second dynamic crosslinking network, thus enhancing the structural stability post-extrusion. With a decrease in ACR level, the fidelity of POS-1/0.67-*y*%CS declined, resulting in a rougher surface and broken filaments. Furthermore, their filaments were prone to breakage during nozzle movement, likely due to a decrease in thixotropy.

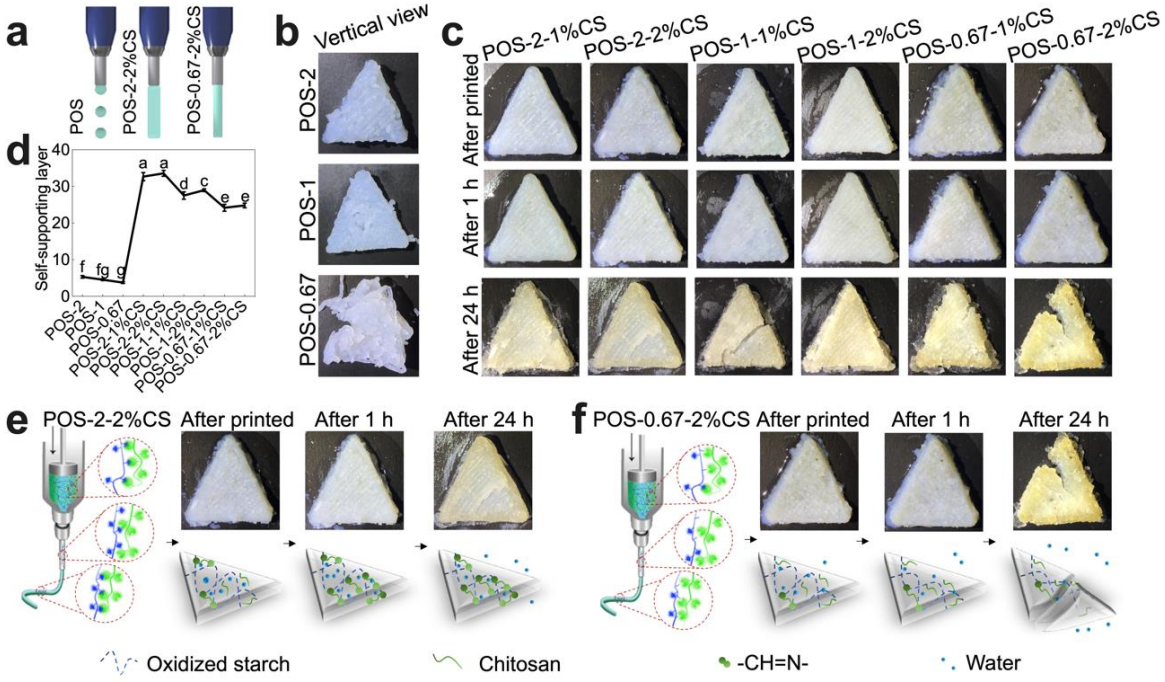

Figure 5. Extrusion process (a), vertical views (b, c), self-supporting layer (d), and molecular motion during extrusion (e, f) of POS/POSC hydrogels.

On the contrary, the surface of POS-2-*y*%CS (especially when $y = 2$) remained flat

even after being stored at room temperature for 1 h, 24 h, or even 7 days, and retained water molecules in the inner structure (**Figure S5**) for 7 days. However, the surface of POS-1/0.67-*y*%CS became rougher and brittle, deteriorating and breaking after 24 h of storage. In addition, the surface of the POSC (especially $x = 1$ and 0.67) hydrogels started to turn yellow due to retrogradation and water loss of the starch. Moreover, the number of self-supporting layers (**Figure 5d** and **Table S5**) of POSC, especially at $x = 2$ and $y = 2$, was significantly higher compared to POS and the other POSC ($p<0.05$), due to its superior structural resilience (Nishiguchi & Taguchi, 2020). This resilience can be attributed to the sufficient Schiff base reaction between the interconnecting OS and CS, forming dynamic covalent crosslinks that preserve the structural integrity (**Figure 6e–6f**).

3.5 Structures of POS/POSC hydrogels

The crosslinking process of molecular chains in the printing environment significantly affects 3D printing properties. As shown in **Figure S6a**, the *CI* after printing of POS-2-*y*%CS, especially $y = 2$, surpassed 75%, suggesting substantial rearrangement of CS and OS molecular chains during the extrusion stage. This rearrangement promoted the Schiff base reaction, generating more dynamic chemical bonds (Farooq et al., 2023). Conversely, the *CI* after printing of POS-1/0.67-*y*%CS was notably lower. For instance, the *CI* after printing of POS-0.67-2%CS exhibited a reduction of 59.12% (from 76.13% to 31.12%) when compared to POS-2-2%CS, indicating a reduced crosslinking. During storage, the *CI* after 1 h of POS-2-1%CS and POS-2-2%CS reached 75% and over 90%, respectively, significantly higher than their *CI* before and after printing. This suggested the formation of additional Schiff base bonds during the storage process. After nozzle shearing, OS and CS molecular chains could rearrange and come into contact, leading to a more dynamic

covalent crosslinking (Mann, Anthony, Agmon, & Appel, 2018). However, the *CI* after 1 h of POS-1/0.67-*y*%CS was significantly lower than their *CI* before and after printing, indicating that the Schiff base bonds failed to re-crosslink to weaken the physical entanglement between CS and OS with a low ACR level during storage.

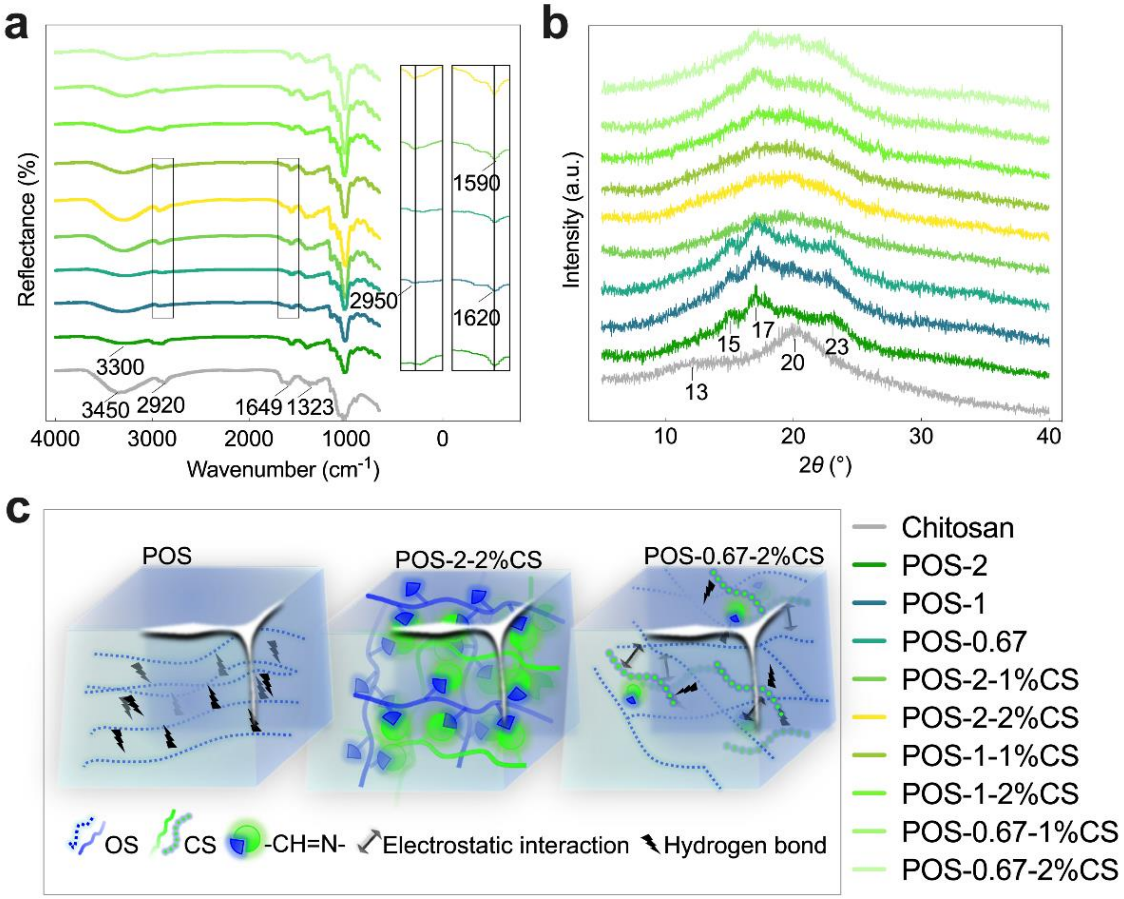

Figure 6. Infrared spectra (a), XRD spectra (b), and schematic distribution of molecular chains (c) of POS/POSC hydrogels.

The FTIR (**Figure 6a**) revealed specific absorption peaks for different components. CS exhibited the primary amino absorption peak (3450 cm^{-1}), an -OH absorption peak (2920 cm^{-1}), and an amide-I absorption peak (1649 cm^{-1}). Meanwhile, POS displayed -OH absorption peaks (3300 cm^{-1}) and a -C=O absorption peak (1620 cm^{-1}). During 3D printing, the absorption peak of -NH_2 (1649 cm^{-1}) and the absorption peak of -C=O (1620 cm^{-1}) in

POSC gradually vanished, and the hydroxyl absorption peaks spanning from 3700 cm^{-1} to 3000 cm^{-1} also changed, indicating the successful integration of OS and CS (Guan et al., 2023). Specifically, new absorption peaks at 1590 cm^{-1} and 2950 cm^{-1} (-C=N-) were observed in POSC, confirming the Schiff base reaction between OS and CS (Guan et al., 2023). Moreover, it was observed that the peak intensity was stronger in POSC-2-2%CS, indicating a higher formation of dynamic covalent crosslinks of Schiff bases. The second-order derivative method (Gieroba et al., 2020) was used to amplify the C-O-H absorption peaks of hydrogels in the range from 980 cm^{-1} to 1030 cm^{-1} (**Figure S6b**). In POS samples, the C-O-H absorption peak at 991 cm^{-1} shifted to a shorter wavelength with decreasing ACR levels, indicating that the strong hydrogen bonds between the carboxyl groups and hydroxyl groups partially replaced the original hydrogen bonds in the starch molecule. The long-range ordered structures were further determined (**Figure 6b**). POS showed diffraction peaks at 2θ = 15° (hkl = 120), 17° (hkl = 012), and 23° (hkl = 131), which corresponded to the A-type crystalline structure (Wang & Wang, 2003), while CS exhibited diffraction peaks at 2θ = 13° (hkl = 011) and 20° (hkl = 121). However, POS-2-*y*% exhibited diffraction peaks at 2θ = 13–25°, indicating that CS and OS formed new dynamic covalent crosslinks through Schiff base reaction after breaking off their own intramolecular and intermolecular hydrogen bonds (Aghajan et al., 2020). At this point, they had good compatibility. However, there were diffraction peaks in POS-1-*y*%CS and POSC-0.67-*y*%CS with low ACR contents, resulting in microphase separation to form separate crystals, respectively (Khalfa et al., 2021). Moreover, this phenomenon was more pronounced with increasing CS addition.

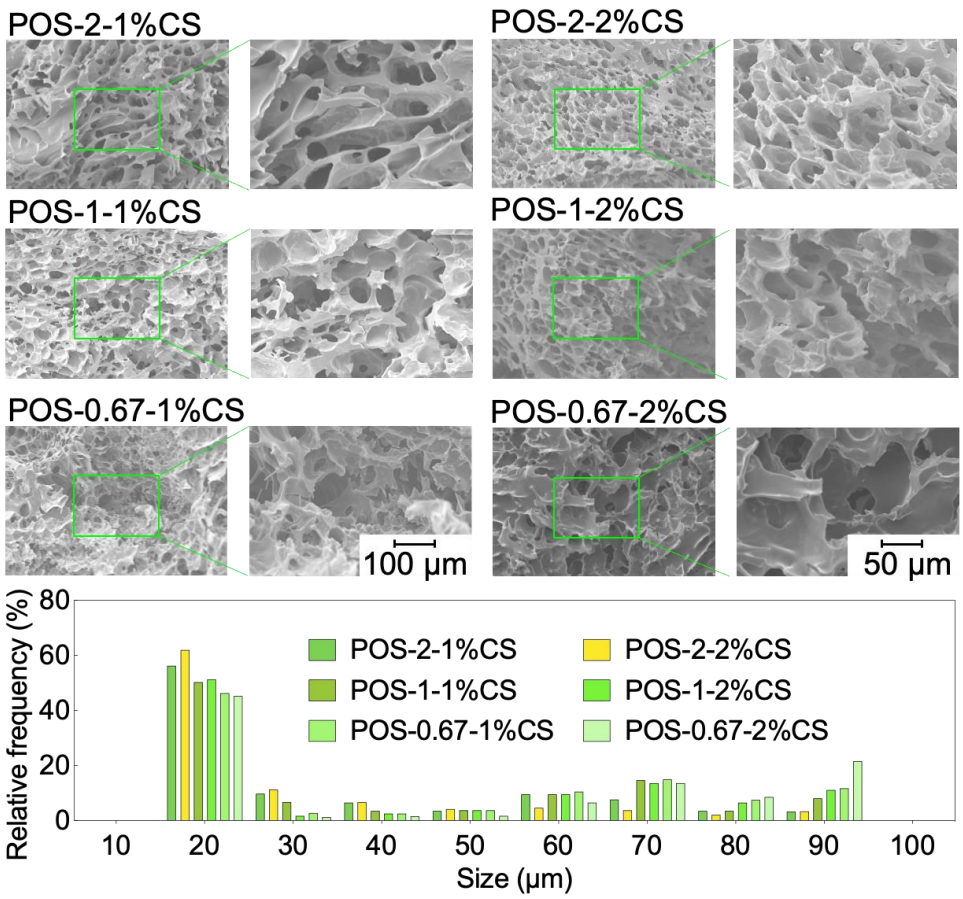

Figure 7. SEM images and pore diameter of POS/POSC hydrogels after printing.

The microstructure of the lyophilized hydrogels was observed by SEM **(Figure 7** and **Figure S6c**), ensuring network stability (Li et al., 2017). POSC-0.67-*y*%CS, with a low ACR content, showed severe aging and formed fragile lamellar structures. This can be attributed to the uneven crosslinking of OS and CS in the hydrogels, resulting from the decrease in the ACR to reduce the density of the crosslinking network. Among POSC samples, POS-2-*y*%CS with high ACR content exhibited fewer surface faults with a highly oriented and tightly ordered pore-like network (**Figure 6c**). With increasing CS content, OS and CS molecules underwent reorientation and complete fusion during the self-supporting phase in POS-2-2%CS. This reorientation facilitated the interaction between the active carbonyl groups and the amino groups, leading to the creation of additional

dynamic Schiff-base crosslinking to form a denser and more continuous network structure (Shahbazi & Jäger, 2020). As a result, POS-2-2%CS hydrogels exhibited a higher number of micropores and demonstrated enhanced structural stability. This network structure with small pores but high porosity could enhance the capillary action between the micropores, thus dramatically increasing the hydration capacity of starch hydrogels (Luo, Dong, Wang, Li, & Xiong, 2021). While POSC (x = 1 and 0.67) hydrogels displayed more macropores and showed decreased structural stability. During 24 h of storage, POS-2-y%CS, especially POS-2-2%CS, could maintain compact and dense cluster-like structures because of better network continuity.

3.6 Mechanical properties of POS/POSC hydrogels

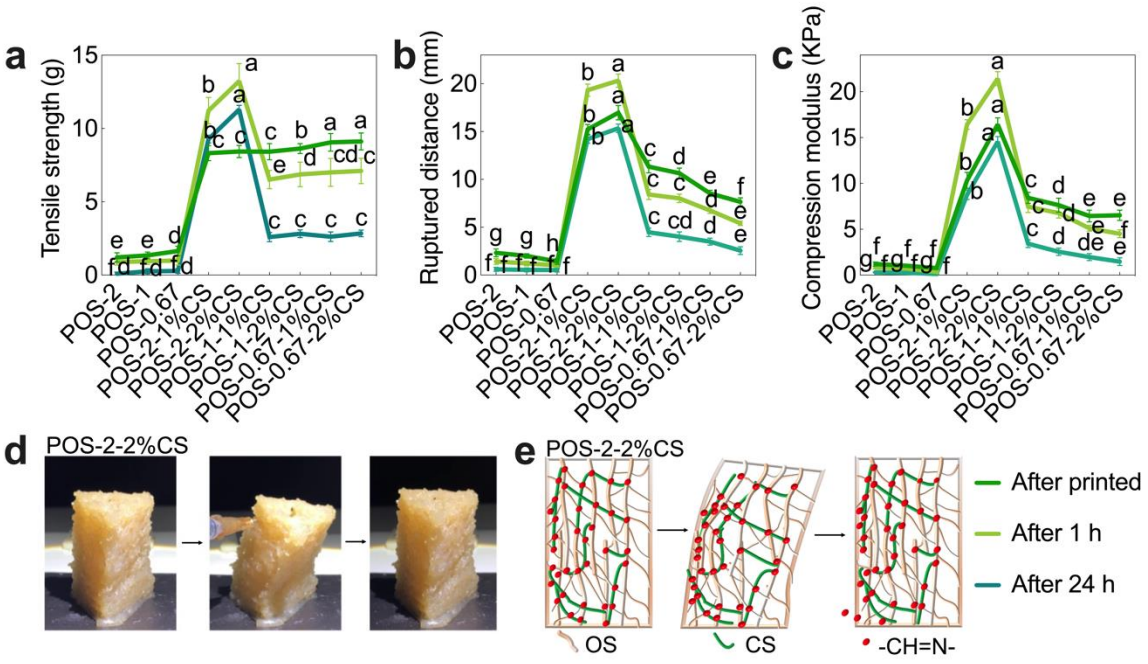

Figure 8. Tensile (a, b), compression (c), and tilt test with its schematic (d, e) of POS/POSC hydrogels.

Mechanical properties played a crucial role in evaluating 3D-printed hydrogels, especially for targeted delivery of drugs to human tissues with different modulus

494 requirements. Due to the limitations of single physical crosslinking, the tensile strength of
495 POS (**Figure 8a** and **Table S6**) ranged from 1.25 g to 1.62 g. However, the addition of CS
496 significantly boosted the tensile strength of POSC. Notably, the tensile strength of POS
497 hydrogels decreased after 1 h storage and especially after 24 h storage, which could be
498 attributed to starch retrogradation. Moreover, tensile strength after 1 h and 24 h storage
499 exhibited a similar trend to POSC, peaking at 13.10 g and 11.29 g for POS-2-2%CS,
500 respectively. This increase was even more prominent in ruptured distance after 1 h and 24
501 h storage (**Figure 8b** and **Table S6**), indicating excellent ductility and toughness. The
502 trends of compressive modulus values (**Figure 8c** and **Table S6**) across all hydrogels
503 mirrored those in the tensile mode. Specifically, POS-2-2%CS exhibited compressive
504 modulus as high as 16.42 kPa (after printing), 21.46 kPa (1 h storage), and 14.55 kPa (24
505 h storage) respectively, surpassing POS and the other POSC samples. As detailed in the
506 section on crosslinking interactions during extrusion, the thorough mixing of OS with CS
507 molecules in the nozzle extrusion environment, coupled with the formation of more
508 dynamic covalent crosslinks of Schiff bases during the subsequent self-supporting phase.
509 All these effects resulted in an increased degree of crosslinking of the hydrogels, which led
510 to denser crosslinking from micropores to micropores, thus exhibiting higher mechanical
511 strength (**Figure 8d–8e**). These effects correlated positively with the increase of the active
512 carbonyl content and the CS addition (Wu et al., 2020).

513 **3.7 Hydration, self-healing, and pH response capacity of POS/POSC hydrogels**

514 The hydration capacity was examined to understand the impact of internal water on
515 the integrity of the hydrogel network structure. As shown in **Figure 9a** and **Table S7**, all
516 POS hydrogels exhibited high T_{22} values, suggesting that a pure, physically crosslinked

hydrogel network was too weak to maintain water retention capabilities. The T_{22} values of POSC samples with CS addition were considerably lower than those of POS, indicating that the introduction of CS facilitated physical entanglement and crosslinking effects, improving moisture retention. Among them, the lower T_{22} values of POS-1/0.67-*y*%CS could be attributed to the presence of increased hydrophilic carboxyl groups (Fan et al., 2023). The T_{22} peak area serves to represent the semi-bonded water ratio. The T_{22} peak area values of POS hydrogels ranged from 85.48% to 90.25%. With the addition of CS and the increase in ACR level, the T_{22} peak area value of POS-2-*y*%CS peaked at 98.02% to 98.20%, significantly higher than those of POS-1/0.67-*y*%CS hydrogels. This might be attributed to the ordered arrangement of the network structure with more microporous structures, which facilitated the consistent distribution and retention of water molecules (Guo et al., 2020).

Thermal stability and water dissipation were investigated using DSC (**Figure 9b** and **Table S7**). The structurally disintegrated POS and the loose and porous POS-1/0.67-*y*%CS were more susceptible to collapse, making them prone to absorb heat and dissipate water. As mentioned above, the peak temperature and ΔH_r (**Table S7**) of POS-2-*y*%CS were significantly higher than the other samples ($p < 0.05$), indicating that the enhanced Schiff base bonds and its induced densification of the dense network improved thermal stability and water retention. From the thermal analysis data (**Figure S7a–S7c** and **Table S8–S9**), POSC hydrogels, especially at $x = 2$ and $y = 2$, exhibited significantly lower weight loss (Phase I and Phase II) than POS, and higher residual weight than POS. This phenomenon also proved that POS-2-*y*%CS, especially POS-2-2%CS hydrogels, displayed enhanced stability and resistance of thermal decomposition during heating. From the obtained results,

the glass transition temperature (T_g) showed a similar trend to that of peak temperature in **Table S7**, reaching a maximum at POS-2-2%CS (103.00 °C). The trends of melting temperature (T_m) were similar to T_g, showing a gradual decrease with the decrease of ACR. This phenomenon confirmed the Schiff Base crosslinking between functional groups within POSC, resulting in a higher T_g and T_m (Elhag et al., 2021).

Water retention was further examined. The results (**Figure 9c**) show that the weight of POS decreased over time, leading to rapid dehydration and structural collapse within 1–2 h. The addition of CS in POSC could improve hydration stability by enhancing water retention. Compared to POS-1-2%CS and POS-0.67-2%CS, POS-2-*y*%CS, with a higher ACR level, exhibited a much longer weightless time (~7 h). In the presence of water, the hydrogen bonds between hydrogel molecules broke, leading to an increase in the volume of intermolecular chain repulsion, while ion-induced electrostatic shielding also led to the destabilization of the hydrogel structure until disintegration (Qin et al., 2019). Further rehydration results show (**Figure 9d**) that the POS saturated and disintegrated structurally in a short time (0.5–1 h), due to the loose network structure and hydrophilic carboxyl groups accelerated the collapse of the hydrogel structure (Zheng et al., 2023). However, the swelling rates of POS-2-*y*%CS gradually increased with time until reaching stability at 3 h (~350% of its weight) and maintained for 7 days, suggesting that the hydrogel network with an orderly arranged structure could enable effective and stable rehydration (**Figure 9e–f**) (Lan, Shi, Xiao, Zhang, & Wang, 2023). Environmental SEM images of the hydrogels after swelling fully and swelling for 7 days were shown in **Figure 9g** and **Figure S8**. POS hydrogels (x = 2, 1, and 0.67, especially 0.67) were easily attacked by water molecules, resulting in larger pores. Compared to POS, POS-2-*y*%CS hydrogels (especially

563 y = 2) demonstrated enhanced stability and continuous water absorption capabilities owing
564 to their smaller micropores and more uniform network structure. Furthermore, the network
565 structure remained homogeneous and stable even after absorption for 7 days. In contrast,
566 the other POSC hydrogels, especially the POS-0.67-y%CS hydrogel, exhibited significant
567 pore enlargement during swelling, leading to a loose and discontinuous network structure.
568 The self-healing experiments (**Figure 9h–9i** and **Figure S9**) demonstrate that the
569 interfacial fusion of POS-x-2%CS, particularly POS-0.67-2%CS, was not evident.
570 However, the blue portion of POS-2-2%CS diffused into the white portion rapidly at 0.5 h
571 and more integrated at 24 h. This phenomenon could be due to the diffusion based on the
572 concentration gradient of blue pigment, viz., Fickian diffusion, indicating the hydrogels
573 likewise stuck together (Li et al., 2024). Considering the possible structural collapse of
574 hydrogels containing Schiff base bonds in an aqueous environment (Liang et al., 2019), we
575 further assessed the release and pH responsiveness of hydrogels loaded with a model drug
576 in pH 7.4/pH 5.0 PBS, and the calibration curve for catechin release was shown in **Figure**
577 **S10a**. Natural compounds, such as catechins, which have a polyhydroxyl structure in
578 polyphenols, are viewed as natural medicine because of their excellent antioxidant effects.
579 However, conventional drug carriers suffer from drawbacks such as sudden release, slow
580 degradation, and instability. In this study, catechins can be stabilized in the system by
581 hydrogen bonds interactions or physical encapsulation. In the pH 7.4 environment (**Figure**
582 **9j**), POS-2-y%CS, especially POS-2-2%CS (78.75%) exhibited a higher release rate at 6 h
583 compared to POS-1/0.67-y%CS (63.58%–70.92%), with an extended release time. This
584 phenomenon could be attributed to the denser and more interconnected micropores of the
585 hydrogels, facilitating the uniform distribution and smooth release through diffusion.

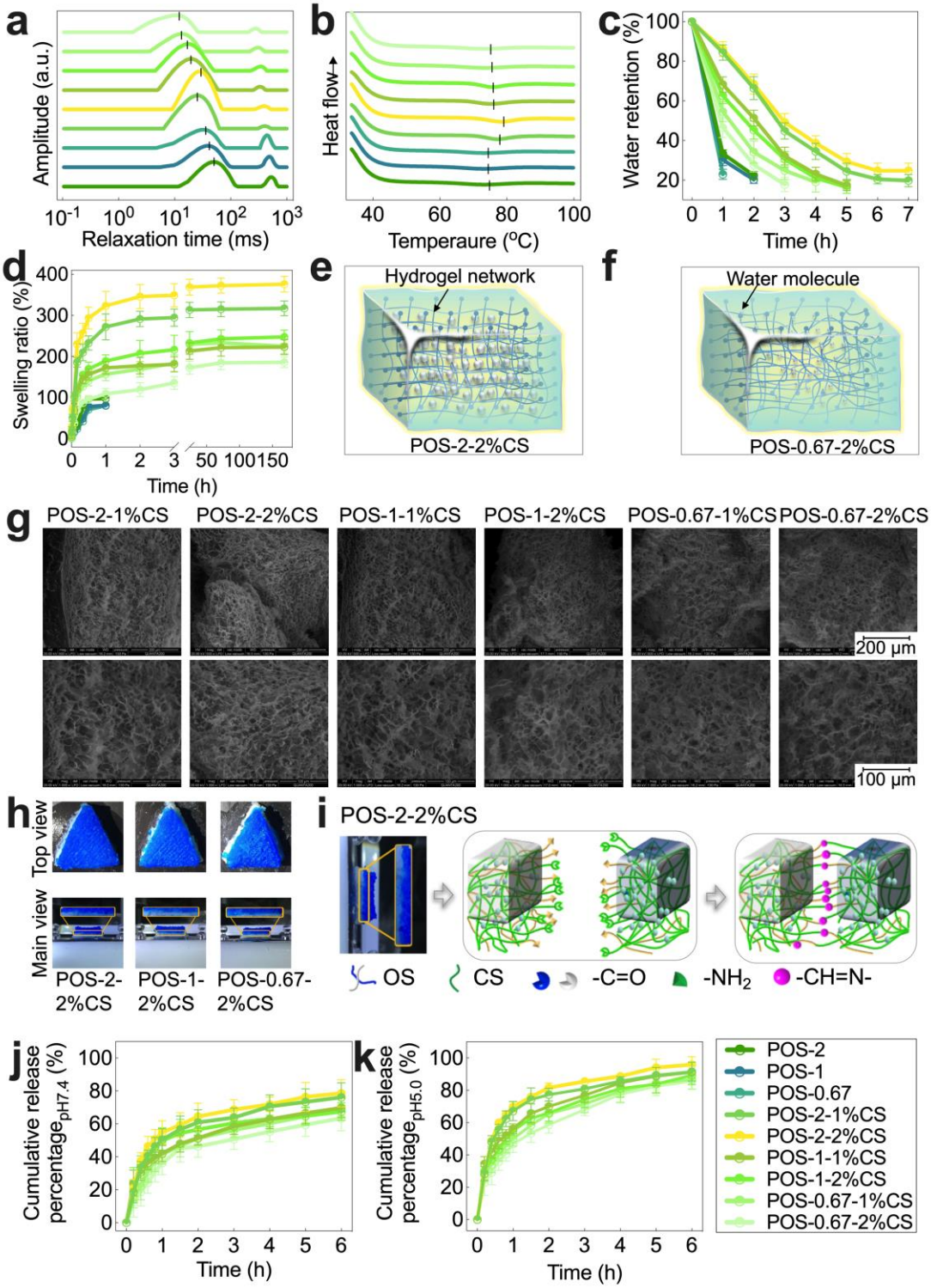

Figure 9. Relaxation (a), DSC spectra (b), water holding (c), swelling curve (d), water holding schematic (e, f), Environmental SEM images after swelling fully (g), self-healing (h, i), and catechin release (j, k) of POS/POSC hydrogels.

In a neutral environment, electrostatic interactions were weakened, resulting in an increased exclusion volume of the molecular chain. This allowed water molecules to easily permeate the hydrogel structure, causing its collapse (Tardy et al., 2021). Notably, considering the potential breakage of Schiff base bonds in an acidic environment (Liang et al., 2022), we evaluated the drug release behavior in pH 5.0 PBS (**Figure 9k**) (Qin et al., 2019). Compared to the typical physiological environment (pH 7.4), POSC released drugs at a faster rate and within a shorter period in the pH 5.0 environment (Taghizadeh et al., 2022). Specifically, POS-2-*y*%CS, especially at $y = 2$, achieved a drug release of over 90% at 6 h. POS-1/0.67-*y*%CS also exhibited high initial drug release (85.96%–88.67%). The protonation of amino groups in CS and carboxyl groups in OS occurred at acidic pH, resulting in the disruption of the original Schiff-based reaction and electrostatic interactions (Ejima et al., 2013; Farris, Song, & Huang, 2010; Guo et al., 2022; Wu et al., 2020). The increased Schiff base reaction in POS-2-2%CS resulted in the expansion of the exclusion space and the subsequent collapse of the loose network for active substance release.

Then the release test for up to 168 h and kinetic fitting at 0 h –6 h were carried out. Based on the results (**Figure S10b-S10c**), the trends of cumulative release after 6h were increase slightly, reaching a peak at POS-2-*y*%CS (particularly at $y = 2$), irrespective of whether the release occurred at pH 7.4 or pH 5.0. Further, zero-order, first-order, Hixson-Crowell, Higuchi, and Korsmeyer-Peppas models were used to fit catechin release at pH 7.4 and pH 5.0, respectively, as shown in **Figure S10d**–**S10g**, and the correlation coefficient (R^2) was shown in **Table S10**. The Korsmeyer-Peppas model showed the best fitting for POSC (R^2 ranged from 0.9817 to 0.9992). When POSC was placed in an acidic or neutral environment, the porous network structure resulted in fast drug diffusion. Thus,

613 the release of the active drug in POSC included both drug diffusion and structural
614 relaxation (Wahab & Janaswamy, 2024). Notably, the enhanced crosslinking in POS-2-
615 *y*%CS contributed to its structural stability over an extended period. Meanwhile, its higher
616 swelling ratio led to a weaker diffusion resistance, which contributed to the sustained drug
617 diffusion of the active substance.

618 **4. Conclusion**

619 This study introduces an innovative approach to fabricating high-performance
620 hydrogels (POSC) through a mixture of CS and OS with varying levels of ACR. Three OS
621 with different ACR levels but insignificant differences in carbonyl + carboxyl content,
622 molecular weight, structure, and properties were first prepared by controlling the oxidizing
623 conditions of the NaClO system. Compared with the single 3D-printed OS, POSC
624 exhibited outstanding printing capabilities and mechanical properties attributed to the
625 dynamic Schiff base crosslinking reaction. It was observed that POSC with lower ACR
626 levels (1 and 0.67) displayed inadequate thixotropy, structural recovery, and post-print
627 crosslinking, resulting in reduced printability and mechanical properties. This deficiency
628 arose from the insufficient content of active carbonyl groups, hindering the formation of
629 an effective Schiff base crosslinking network. Conversely, due to sufficient dynamic Schiff
630 base crosslinking, POSC with an ACR level of 2:1 (referred to as POS-2-*y*%CS)
631 demonstrated enhanced shear-thinning behavior and thixotropic attributes. During the post-
632 printing stage, the Schiff base crosslinking in POSC was further strengthened, resulting in
633 improved shape fidelity and mechanical properties, including a remarkable structural
634 recovery rate of 95% and self-healing ability. The superior performance was more
635 pronounced with increasing CS content (as seen in POS-2-2%CS), which could be stored

stably for 7 days. This was due to more dynamic crosslinking of Schiff bases, resulting in a denser more continuous network structure and smaller pore size of the POS-2-2%CS hydrogel. Moreover, it exhibited long-term stability during water loss and rehydration, as well as enhanced resistance to thermal decomposition. Due to these advantages, its potential applications included sustained release in solutions of varying pH, and pH-responsive release and sustained drug diffusion of the active substance. Overall, this study provided an innovative method for designing 3D-printed biopolymer hydrogels with excellent printability and mechanical properties.

Acknowledgements

This research has been financially supported by the National Natural Science Foundation of China (32372276).

Declaration of competing interest

The authors declare to have no conflict of interest.

CRediT authorship contribution statement

Junchao Zhu: Data curation, Formal analysis, Investigation, Methodology, Writing – original draft; **Fengwei Xie**: Conceptualization, Formal analysis, Supervision, Writing – review & editing. **Zhipeng Qiu**: Conceptualization, Data curation, Formal analysis, Investigation, Methodology, Supervision, Writing – review & editing; **Ling Chen**: Conceptualization, Funding acquisition, Investigation, Project administration, Resources Supervision, Writing – review & editing.

Supporting Information

Additional figures and tables including preparation, measurement, characterizations of starches (**Figure S1—S2** and **Table S1**), rheological (**Figure S3—S4** and **Table S2—**

S5), hydrogel images (**Figure S5**), structure (**Figure S6**), mechanical strength (**Table S6**), and hydration, water-holding and thermal properties (**Figure S7**—**S8** and **Table S7**—**S9**), self-healing performance (**Figure S9**)and catechin release (**Figure S10** and **Table S10**) of hydrogels.

References

Aghajan, M. H., Panahi-Sarmad, M., Alikarami, N., Shojaei, S., Saeidi, A., Khonakdar, H. A., Shahrousvan, M., & Goodarzi, V. (2020). Using solvent-free approach for preparing innovative biopolymer nanocomposites based on PGS/gelatin. *European Polymer Journal,* 131, 109720.

Ahn, D., Stevens, L. M., Zhou, K., & Page, Z. A. (2020). Rapid High-Resolution Visible Light 3D Printing. *ACS Central Science,* 6(9), 1555-1563.

Antony, R., Arun, T., & Manickam, S. T. D. (2019). A review on applications of chitosan-based Schiff bases. *International Journal of Biological Macromolecules,* 129, 615-633.

Balaji, A. B., Pakalapati, H., Khalid, M., Walvekar, R., & Siddiqui, H. (2018). Natural and synthetic biocompatible and biodegradable polymers. *Biodegradable and biocompatible polymer composites,* 286, 3-32.

Bao, X., Yu, L., Shen, S., Simon, G. P., Liu, H., & Chen, L. (2019). How rheological behaviors of concentrated starch affect graft copolymerization of acrylamide and resultant hydrogel. *Carbohydrate Polymers,* 219, 395-404.

Bryant, W. M. D., & Smith, D. M. (1935). Improved Hydroxylamine Method for the Determination of Aldehydes and Ketones. Displacement of Oxime Equilibria by Means of Pyridine. *Journal of the American Chemical Society,* 57(1), 57-61.

682 Chatterjee, C., Pong, F., & Sen, A. (2015). Chemical conversion pathways for
683 carbohydrates. *Green Chemistry,* 17(1), 40-71.
684 Chen, X., Yan, S., Wang, H., Hu, Z., Wang, X., & Huo, M. (2015a). Aerobic oxidation of
685 starch catalyzed by isopolyoxovanadate Na4Co (H2O) 6V10O28. *Carbohydrate*
686 *Polymers,* 117, 673-680.
687 Chen, X., Yan, S., Wang, H., Hu, Z., Wang, X., & Huo, M. (2015b). Aerobic oxidation of
688 starch catalyzed by isopolyoxovanadate Na4Co(H2O)6V10O28. *Carbohydrate*
689 *Polymers,* 117, 673-680.
690 Cheng, X., Wang, S., Huang, W., Wang, F., Fang, S., Ge, R., Zhang, Q., Zhang, L., Du, W.,
691 & Fang, F. (2022). Current status of hypochlorite technology on the wastewater
692 treatment and sludge disposal: Performance, principals and prospects. *Science of*
693 *The Total Environment,* 803, 150085.
694 Cui, T., Wu, Y., Ni, C., Sun, Y., & Cheng, J. (2022). Rheology and texture analysis of
695 gelatin/dialdehyde starch hydrogel carriers for curcumin controlled release.
696 *Carbohydrate Polymers,* 283, 119154.
697 Dence, C. (1992). *Determination of carboxyl groups*. In *Methods in lignin chemistry* (pp.
698 458-464): Springer
699 Ejima, H., Richardson, J. J., Liang, K., Best, J. P., van Koeverden, M. P., Such, G. K., Cui,
700 J., & Caruso, F. (2013). One-Step Assembly of Coordination Complexes for
701 Versatile Film and Particle Engineering. *Science,* 341(6142), 154-157.
702 Elhag, M., Abdelwahab, H. E., Mostafa, M. A., Yacout, G. A., Nasr, A. Z., Dambruoso, P.,
703 & El Sadek, M. M. (2021). One pot synthesis of new cross-linked chitosan-
704 Schiff'base: Characterization, and anti-proliferative activities. *International*

Journal of Biological Macromolecules, 184, 558-565.

Fan, X., Zhang, R., Sui, S., Liu, X., Liu, J., Shi, C., Zhao, N., Zhong, C., & Hu, W. (2023). Starch‐Based Superabsorbent Hydrogel with High Electrolyte Retention Capability and Synergistic Interface Engineering for Long‐Lifespan Flexible Zinc− Air Batteries. *Angewandte Chemie International Edition,* 62(22), e202302640.

Farooq, S., Ahmad, M. I., Zhang, Y., & Zhang, H. (2023). Impact of interfacial layer number and Schiff base cross-linking on the microstructure, rheological properties and digestive lipolysis of plant-derived oil bodies-based oleogels. *Food Hydrocolloids,* 138, 108473.

Farris, S., Song, J., & Huang, Q. (2010). Alternative Reaction Mechanism for the Cross-Linking of Gelatin with Glutaraldehyde. *Journal of Agricultural and Food Chemistry,* 58(2), 998-1003.

Gieroba, B., Sroka-Bartnicka, A., Kazimierczak, P., Kalisz, G., Lewalska-Graczyk, A., Vivcharenko, V., Nowakowski, R., Pieta, I. S., & Przekora, A. (2020). Spectroscopic studies on the temperature-dependent molecular arrangements in hybrid chitosan/1, 3-β-D-glucan polymeric matrices. *International Journal of Biological Macromolecules,* 159, 911-921.

Guan, X., Zhang, B., Li, D., Ren, J., Zhu, Y., Sun, Z., & Chen, Y. (2023). Semi-unzipping of chitosan-sodium alginate polyelectrolyte gel for efficient capture of metallic mineral ions from tannery effluent. *Chemical Engineering Journal,* 452, 139532.

Guo, B., Liang, Y., & Dong, R. (2023). Physical dynamic double-network hydrogels as dressings to facilitate tissue repair. *Nature Protocols,* 18(11), 3322-3354.

Guo, Y., Bae, J., Fang, Z., Li, P., Zhao, F., & Yu, G. (2020). Hydrogels and hydrogel-derived materials for energy and water sustainability. *Chemical Reviews,* 120(15), 7642-7707.

Guo, Y., Zhou, Q., Nan, J., Shi, W., Cui, F., & Zhu, Y. (2022). Perylenetetracarboxylic acid nanosheets with internal electric fields and anisotropic charge migration for photocatalytic hydrogen evolution. *Nature Communications,* 13(1), 2067.

Hafeez, S., Aldana, A. A., Duimel, H., Ruiter, F. A. A., Decarli, M. C., Lapointe, V., van Blitterswijk, C., Moroni, L., & Baker, M. B. (2023). Molecular Tuning of a Benzene-1,3,5-Tricarboxamide Supramolecular Fibrous Hydrogel Enables Control over Viscoelasticity and Creates Tunable ECM-Mimetic Hydrogels and Bioinks. *Advanced Materials,* 35(24), 2207053.

Haq, F., Yu, H., Wang, L., Teng, L., Haroon, M., Khan, R. U., Mehmood, S., Ullah, R. S., Khan, A., & Nazir, A. (2019). Advances in chemical modifications of starches and their applications. *Carbohydrate research,* 476, 12-35.

Huang, X., Li, X., Chen, L., & Li, L. (2017). Spermine modified starch-based carrier for gene delivery: Structure-transfection activity relationships. *Carbohydrate Polymers,* 173, 690-700.

Jia, Y., & Li, J. (2015). Molecular assembly of Schiff base interactions: construction and application. *Chemical Reviews,* 115(3), 1597-1621.

Kácerová, S., Muchová, M., Doudová, H., Münster, L., Hanulíková, B., Valásková, K., Kaspárková, V., Kuritka, I., Humpolícek, P., Víchová, Z., Vasícek, O., & Vícha, J. (2024). Chitosan/dialdehyde cellulose hydrogels with covalently anchored polypyrrole: Novel conductive, antibacterial, antioxidant, immunomodulatory, and

anti-inflammatory materials. *Carbohydrate Polymers,* 327, 121640.

Kang, D.-H., Louis, F., Liu, H., Shimoda, H., Nishiyama, Y., Nozawa, H., Kakitani, M., Takagi, D., Kasa, D., & Nagamori, E. (2021). Engineered whole cut meat-like tissue by the assembly of cell fibers using tendon-gel integrated bioprinting. *Nature Communications,* 12(1), 5059.

Kato, Y., Matsuo, R., & Isogai, A. (2003). Oxidation process of water-soluble starch in TEMPO-mediated system. *Carbohydrate Polymers,* 51(1), 69-75.

Khalfa, A. L., Becker, M. L., & Dove, A. P. (2021). Stereochemistry-Controlled Mechanical Properties and Degradation in 3D-Printable Photosets. *Journal of the American Chemical Society,* 143(42), 17510-17516.

Kizil, R., Irudayaraj, J., & Seetharaman, K. (2002). Characterization of irradiated starches by using FT-Raman and FTIR spectroscopy. *Journal of Agricultural and Food Chemistry,* 50(14), 3912-3918.

Lan, J., Shi, L., Xiao, W., Zhang, X., & Wang, S. (2023). A Rapid Self-Pumping Organohydrogel Dressing with Hydrophilic Fractal Microchannels to Promote Burn Wound Healing. *Advanced Materials,* 35(38), 2301765.

Lee, S. C., Gillispie, G., Prim, P., & Lee, S. J. (2020). Physical and Chemical Factors Influencing the Printability of Hydrogel-based Extrusion Bioinks. *Chemical Reviews,* 120(19), 10834-10886.

Li, D.-q., Tohti, M., Fu, Y.-s., Zhang, Y., Xiong, Z.-w., Li, J., & Guo, Y.-F. (2024). Aldehyde group pendant-grafted pectin-based injectable hydrogel. *International Journal of Biological Macromolecules,* 264, 130453.

Li, H., Tan, Y. J., Leong, K. F., & Li, L. (2017). 3D Bioprinting of Highly Thixotropic

774 Alginate/Methylcellulose Hydrogel with Strong Interface Bonding. *ACS Applied*
775 *Materials & Interfaces,* 9(23), 20086-20097.
776 Li, J., Wu, C., Chu, P. K., & Gelinsky, M. (2020). 3D printing of hydrogels: Rational design
777 strategies and emerging biomedical applications. *Materials Science and*
778 *Engineering: R: Reports,* 140, 100543.
779 Liang, Y., Li, M., Yang, Y., Qiao, L., Xu, H., & Guo, B. (2022). pH/glucose dual responsive
780 metformin release hydrogel dressings with adhesion and self-healing via dual-
781 dynamic bonding for athletic diabetic foot wound healing. *ACS nano,* 16(2), 3194-
782 3207.
783 Liang, Y., Zhao, X., Hu, T., Chen, B., Yin, Z., Ma, P. X., & Guo, B. (2019). Adhesive
784 hemostatic conducting injectable composite hydrogels with sustained drug release
785 and photothermal antibacterial activity to promote full‐thickness skin
786 regeneration during wound healing. *Small,* 15(12), 1900046.
787 Lu, F., Wang, Y., Wang, C., Kuga, S., Huang, Y., & Wu, M. (2020). Two-Dimensional
788 Nanocellulose-Enhanced High-Strength, Self-Adhesive, and Strain-Sensitive
789 Poly(acrylic acid) Hydrogels Fabricated by a Radical-Induced Strategy for a Skin
790 Sensor. *ACS Sustainable Chemistry & Engineering,* 8(8), 3427-3436.
791 Luo, H., Dong, F., Wang, Q., Li, Y., & Xiong, Y. (2021). Construction of porous starch-
792 based hydrogel via regulating the ratio of amylopectin/amylose for enhanced water-
793 retention. *Molecules,* 26(13), 3999.
794 Mandala, I. G., & Bayas, E. (2004). Xanthan effect on swelling, solubility and viscosity of
795 wheat starch dispersions. *Food Hydrocolloids,* 18(2), 191-201.
796 Mann, J. L., Anthony, C. Y., Agmon, G., & Appel, E. A. (2018). Supramolecular polymeric

797 biomaterials. *Biomaterials science,* 6(1), 10-37.
798 Mea, H. J., Delgadillo, L., & Wan, J. (2020). On-demand modulation of 3D-printed
799 elastomers using programmable droplet inclusions. *Proceedings of the National*
800 *Academy of Sciences,* 117(26), 14790-14797.
801 Moorthy, S. N. (1985). Effect of different types of surfactants on cassava starch properties.
802 *Journal of Agricultural and Food Chemistry,* 33(6), 1227-1232.
803 Narupai, B., Smith, P. T., & Nelson, A. (2021). 4D printing of multi‐stimuli responsive
804 protein‐based hydrogels for autonomous shape transformations. *Advanced*
805 *Functional Materials,* 31(23), 2011012.
806 Nishiguchi, A., & Taguchi, T. (2020). A Thixotropic, Cell-Infiltrative Nanocellulose
807 Hydrogel That Promotes in Vivo Tissue Remodeling. *ACS Biomaterials Science &*
808 *Engineering,* 6(2), 946-958.
809 Pérez, S., Baldwin, P. M., & Gallant, D. J. (2009). *Structural features of starch granules I*.
810 In *Starch* (pp. 149-192): Elsevier
811 Qin, Y., Wang, J., Qiu, C., Hu, Y., Xu, X., & Jin, Z. (2019). Self-Assembly of Metal–
812 Phenolic Networks as Functional Coatings for Preparation of Antioxidant,
813 Antimicrobial, and pH-Sensitive-Modified Starch Nanoparticles. *ACS Sustainable*
814 *Chemistry & Engineering,* 7(20), 17379-17389.
815 Qiu, Z., Zeng, X., Xu, J., Zheng, B., & Chen, L. (2023). Regioselective C6-OH oxidation
816 of starch by laccase-TEMPO-system: A multi-scale structure evolution and water
817 absorption properties study. *Industrial Crops and Products,* 193, 116148.
818 Qiu, Z., Zheng, B., Xu, J., Chen, J., & Chen, L. (2022). 3D-printing of oxidized starch-
819 based hydrogels with superior hydration properties. *Carbohydrate Polymers,* 292,

119686.

RUTENBERG, M. W., & SOLAREK, D. (1984). *Starch derivatives: Production and uses*. In *Starch: Chemistry and technology* (pp. 311-388): Elsevier

Schwab, A., Levato, R., D'Este, M., Piluso, S., Eglin, D., & Malda, J. (2020). Printability and Shape Fidelity of Bioinks in 3D Bioprinting. *Chemical Reviews,* 120(19), 11028-11055.

Seoane-Viaño, I., Januskaite, P., Alvarez-Lorenzo, C., Basit, A. W., & Goyanes, A. (2021). Semi-solid extrusion 3D printing in drug delivery and biomedicine: Personalised solutions for healthcare challenges. *Journal of Controlled Release,* 332, 367-389.

Serrero, A., Trombotto, S., Cassagnau, P., Bayon, Y., Gravagna, P., Montanari, S., & David, L. (2010). Polysaccharide Gels Based on Chitosan and Modified Starch: Structural Characterization and Linear Viscoelastic Behavior. *Biomacromolecules,* 11(6), 1534-1543.

Shahbazi, M., & Jäger, H. (2020). Current status in the utilization of biobased polymers for 3D printing process: a systematic review of the materials, processes, and challenges. *ACS Applied Bio Materials,* 4(1), 325-369.

Shokri, Z., Seidi, F., Saeb, M. R., Jin, Y., Li, C., & Xiao, H. (2022). Elucidating the impact of enzymatic modifications on the structure, properties, and applications of cellulose, chitosan, starch and their derivatives: a review. *Materials Today Chemistry,* 24, 100780.

Soleymani Eil Bakhtiari, S., Bakhsheshi-Rad, H. R., Karbasi, S., Razzaghi, M., Tavakoli, M., Ismail, A. F., Sharif, S., RamaKrishna, S., Chen, X., & Berto, F. (2021). 3-Dimensional Printing of Hydrogel-Based Nanocomposites: A Comprehensive

Review on the Technology Description, Properties, and Applications. *Advanced Engineering Materials,* 23(10), 2100477.

Taghizadeh, M., Taghizadeh, A., Yazdi, M. K., Zarrintaj, P., Stadler, F. J., Ramsey, J. D., Habibzadeh, S., Rad, S. H., Naderi, G., & Saeb, M. R. (2022). Chitosan-based inks for 3D printing and bioprinting. *Green Chemistry,* 24(1), 62-101.

Tardy, B. L., Mattos, B. D., Otoni, C. G., Beaumont, M., Majoinen, J., Kämäräinen, T., & Rojas, O. J. (2021). Deconstruction and reassembly of renewable polymers and biocolloids into next generation structured materials. *Chemical Reviews,* 121(22), 14088-14188.

Tolvanen, P., Mäki-Arvela, P., Sorokin, A. B., Salmi, T., & Murzin, D. Y. (2009). Kinetics of starch oxidation using hydrogen peroxide as an environmentally friendly oxidant and an iron complex as a catalyst. *Chemical Engineering Journal,* 154(1), 52-59.

Varma, C. A. K., & Kumar, K. J. (2017). Structural, functional and pH sensitive release characteristics of water-soluble polysaccharide from the seeds of Albizia lebbeck L. *Carbohydrate Polymers,* 175, 502-508.

Wahab, M., & Janaswamy, S. (2024). Porous corn starch granules as effective host matrices for encapsulation and sustained release of curcumin and resveratrol. *Carbohydrate Polymers*, 121967.

Wang, Y.-J., & Wang, L. (2003). Physicochemical properties of common and waxy corn starches oxidized by different levels of sodium hypochlorite. *Carbohydrate Polymers,* 52(3), 207-217.

Wu, C.-N., & Lai, H.-M. (2019). Novel pH-responsive granules with tunable volumes from oxidized corn starches. *Carbohydrate Polymers,* 208, 201-212.

Wu, M., Chen, J., Huang, W., Yan, B., Peng, Q., Liu, J., Chen, L., & Zeng, H. (2020). Injectable and Self-Healing Nanocomposite Hydrogels with Ultrasensitive pH-Responsiveness and Tunable Mechanical Properties: Implications for Controlled Drug Delivery. *Biomacromolecules,* 21(6), 2409-2420.

Yi, X., Zhang, S., & Ju, B. (2014). Preparation of water‐soluble oxidized starch with high carbonyl content by sodium hypochlorite. *Starch‐Stärke,* 66(1-2), 115-123.

Zhang, X. N., Wang, Y. J., Sun, S., Hou, L., Wu, P., Wu, Z. L., & Zheng, Q. (2018). A Tough and Stiff Hydrogel with Tunable Water Content and Mechanical Properties Based on the Synergistic Effect of Hydrogen Bonding and Hydrophobic Interaction. *Macromolecules,* 51(20), 8136-8146.

Zhao, J., Peng, Y.-Y., Wang, J., Diaz-Dussan, D., Tian, W., Duan, W., Kong, L., Hao, X., & Narain, R. (2022). Temperature-Responsive Aldehyde Hydrogels with Injectable, Self-Healing, and Tunable Mechanical Properties. *Biomacromolecules,* 23(6), 2552-2561.

Zhao, X., Guo, B., Wu, H., Liang, Y., & Ma, P. X. (2018). Injectable antibacterial conductive nanocomposite cryogels with rapid shape recovery for noncompressible hemorrhage and wound healing. *Nature Communications,* 9(1), 2784.

Zhao, X., Liang, Y., Huang, Y., He, J., Han, Y., & Guo, B. (2020). Physical double‐network hydrogel adhesives with rapid shape adaptability, fast self‐healing, antioxidant and NIR/pH stimulus‐responsiveness for multidrug‐resistant bacterial infection and removable wound dressing. *Advanced Functional Materials,* 30(17), 1910748.

Zheng, B., Qiu, Z., Xu, J., Zeng, X., Liu, K., & Chen, L. (2023). 3D printing-mediated

889 microporous starch hydrogels for wound hemostasis. *Journal of Materials*
890 *Chemistry B,* 11(35), 8411-8421.
891

Supporting Information

Effect of Active Carbonyl-Carboxyl Ratio on Dynamic Schiff Base Crosslinking and Its Modulation of High-Performance Oxidized Starch-Chitosan Hydrogels by Hot Extrusion 3D Printing

Junchao Zhu [a], Fengwei Xie [b], Zhipeng Qiu [a, *], Ling Chen [a, **]

[a] *Ministry of Education Engineering Research Center of Starch & Protein Processing, Guangdong Province Key Laboratory for Green Processing of Natural Products and Product Safety, School of Food Science and Engineering, South China University of Technology, Guangzhou 510640, China*.

[b] *School of Engineering, Newcastle University, Newcastle Upon Tyne, NE1 7RU, United Kingdom*

[*] Corresponding author. Email: fesolorway@mail.scut.edu.cn (Z. Qiu)

[**] Corresponding author. Email: felchen@scut.edu.cn (L. Chen)

Supporting measurement of MS/OS

Active carbonyl group measurement

The procedure involved the initial mixing of 4.00 g of MS/OS and 100.00 mL of deionized water in a 100 mL round-bottomed three-necked flask. This mixture was stirred thoroughly and subjected to a reaction at 100 °C with constant stirring at 300 rpm for 30 min. The reaction mixture was then transferred to a water bath maintained at 40 °C and left for 20 min. Subsequently, 15.00 mL of $NH_2OH{\cdot}HCl$ was added into the reaction mixture. The pH of the reaction solution was adjusted to 3.20 using 0.10 M HCl, and the reaction continued for 4 h at 40 °C with continuous stirring at 300 rpm. Finally, the pH was re-adjusted to 3.20 using 0.10 M HCl, and the total amount of HCl was recorded. The active carbonyl group contents were then calculated with the formula (Eq. S1).

$$W_{active\ carbonyl\ groups}\ (\%) = c\ (V_0 - V_1)\ \times\ M_e\ \times\ 100\ /\ m \qquad \text{(Eq. S1)}$$

where c is the molar concentration of HCl (M), V_0 is the volume of HCl consumed by the MS (mL), V_1 is the volume of HCl consumed by OS (mL), M_e is the millimolar mass of active carbonyl group (0.028 g/mM), m is the dry weight of OS (g).

Carboxyl groups measurement

1.00 g of MS/OS and 20.00 mL of 0.10 M HCl were mixed in a 20 mL centrifuge tube, stirred thoroughly, and then reacted at 25 °C and 300 rpm for 30 min. Then, the samples were washed several times until all chloride ions were removed. To ensure the absence of chloride ions in the wash solution, 1.00 mL of $AgNO_3$ was added to 5.00 mL of the wash solution for testing. The washed samples were then combined with 300 mL of deionized water and reacted at 100 °C, 300 rpm for 30 min. After the reaction, 0.50 mL of 0.10 M phenolphthalein was added to the reaction solution. The total amount of NaOH solution

required for titration was recorded. The titration proceeded until the solution turned pink and remained stable for at least half an hour. The carboxyl group content was calculated with the formula (Eq. 2).

$$W_{carboxyl\ groups}\ (\%) = c\ (V_1 - V_0)\ \times\ M_e\ \times\ 100\ /\ m \qquad \text{(Eq. 2)}$$

where c is the molar concentration of NaOH solution (M), V_0 is the volume of NaOH solution consumed by the MS (mL), V_1 is the volume of NaOH solution consumed by OS (mL), M_e is the millimolar mass of carbonyl group (0.045 g/mM), m is the dry weight of OS (g).

FTIR

2.00 g of MS/OS/CS/POS/POSC flour was placed in the OMNI spectral sampler and scanned. The scanning range was 4000 to 400 cm^{-1}, with a resolution of 8 cm^{-1}, and the scanning number was 64 times with the deduction of the air background. Finally, the spectra were deconvoluted and analyzed using OMNIC software.

***M*w**

For each sample, 5 mg of starch was dispersed in 5 mL of dimethyl sulfoxide (DMSO) containing LiBr (50 mM) and then heated at 110 °C for 1 h. Then, the completely dissolved sample solutions were filtered using a 5 μm membrane filter (Millipore Co., USA) and transferred to sample bottles. The GPC system consisted of a pump (1515, Waters, Milford, MA, USA), an auto-injector with a 0.1 mL loop (717, Waters), and three columns (Sytyragel HMW7 GPC column, Sytyragel HMW6E GPC column, and Sytyragel HMW2 GPC column, respectively, 7.8 × 300 mm, Waters) (J. Chen, Li, Chen, & Xie, 2018).

Brabender

First, a 100.00 mL suspension with a 6% mass concentration of starch was prepared

in a 200 mL beaker, stirred thoroughly, and then transferred to a Brabender cup for testing. Throughout the testing process, the stirring speed was maintained at 210 rpm, the temperature range was from 30 to 95 °C, the temperature rate was fixed at 7.5 °C/min, and the stability temperature was 95 °C for 30 min. Peak viscosity was determined by analyzing the spectra using Brabender software.

XRD

The moisture content of MS/OS/CS/POS/POSC flour was adjusted to 5% and then placed in rectangular glass cells. The angle range was 4–40°, the tube pressure was 40 kV, the tube current was 40 mA, the step size was 0.016°, and the scanning speed was 20°/min. Subsequently, the spectra were analyzed using MDI Jade 6.0 and Peakfit 4.12, and the relative crystallinity was then calculated.

DSC

DSC was used at a rate of 10 °C/min within the temperature range of 10 °C to 100 °C (Khalfa, Becker, & Dove, 2021). MS/OS (6.00 mg dry weight) were placed in the high-pressure metal pan and then stored at 4 °C for 12 h to allow for moisture equilibration.

Polarizing microscope

Polarized microscope images of starch (MS/OS) were obtained by a polarizing microscope (Zeiss, Axioskop 40, Germany) equipped with a 35 mm SLA camera (Power Shot G5, Canon, Tokyo, Japan). MS/OS (0.10 g) and glycerol (0.20 ml, to reduce aerosolization and movement of the granules) were placed on a glass slide, covered with a coverslip. Then, the morphology of the starch and the Maltese crosses were observed under normal light and polarized light, respectively, at a magnification of 500×.

Solubility measurement

The 20% w/v starch suspension was stirred at 120 rpm, 50 ^{o}C for 30 min, followed by centrifugation at 5000 rpm for 10 min. The centrifuged supernatant was transferred to an aluminum box and dried at 120 °C for 6 h. Solubility was calculated using the formula (Eq. S3).

$$Solubility\ (\%)\ =\ (1 - A_1\ /\ A_0)\ \times\ 100\% \qquad \text{(Eq. S3)}$$

where A_1 and A_0 are the weights of dried starch and original starch, respectively.

Macro-rheology measurement

Macro-rheology was assessed using a fork and spoon, as described previously (Pematilleke, Kaur, Adhikari, & Torley, 2022): in the fork pressure test, resilience was evaluated by pressing the thumb on the fork placed on top of the POS/POSC inks (equilateral triangles with sides of 15.00 mm) until the nail turned white. In the spoon tilt test, the spoon containing OS/OSC inks was tilted to one side until slipping occurred. In the fork drip test, the spoon with OS/OSC inks was observed to flow over the tines of the fork.

SEM

POSC hydrogels after being stored for 1 h and 24 h were frozen in liquid nitrogen, extracted, and became brittle. Subsequently, they were affixed onto the test plate using conductive tape, followed by gold spraying (Li, Tan, Leong, & Li, 2017). The hydrogels were then observed and photographed by SEM (Zeiss, Merlin EVO18, Germany) at 20 kV and 200/500 magnifications.

Supporting Results and Discussion

Characterization of MS/OS

Compared to MS, the positions and intensities (**Figure S1a**) of the A-type crystalline peaks at 15°, 17°, 18°, and 23° and the V-type crystalline peak at 20° of OS did not change dramatically (Xue, Ma, Yang, & Wei, 2021). Interestingly, compared with MS, OS-2 and OS-1 showed an increasing trend in relative crystallinity, peak temperature, and ΔH_r (**Figure S1b**), which resulted from the hydrolysis of the amorphous structure, leading to a more perfect crystalline structure (Wang & Wang, 2003). However, the relative crystallinity and peak temperature decreased with increased oxidation (ACR level reached 0.67), indicating the onset of oxidation reaction within the crystalline region of the starch granules (Chen et al., 2015; Tolvanen, Mäki-Arvela, Sorokin, Salmi, & Murzin, 2009). Compared to MS, the OS exhibited a more complete particle morphology and displayed the "Maltese cross" (**Figure S2**) in the polarized field of view. Notably, OS-2/OS-1 showed a decrease in granule diameter compared to MS, while OS-0.67 showed a further decrease in diameter and an increase in fragmentation.

Supporting Table

Table S1. Structures and characteristics of MS/OS.

Samples	Active carbonyl (%)	Carboxyl (%)	A + C (%)	ACR	M_w (10^6 g/mol)	Peak viscosity (BU)
MS	-	-	-	-	21.70±0. 590[a]	726.5±7.78[a]
OS-2	1.55±0.03[a]	0.80±0.03[c]	2.35±0.07[a]	2:1	0.916±0.030[b]	629.5±26.36[b]
OS-1	1.25±0.03[b]	1.23±0.06[b]	2.47±0.09[a]	1:1	0.884±0.023[b]	582.5±33.54[b]
OS-0.67	0.98±0.03[c]	1.49±0.06[a]	2.47±0.09[a]	2:3	0.857±0.027[b]	557.0±27.07[b]

A + C, active carbonyl + carboxyl content; *Mw,* molecular weight.

Table S2. pH and rheological characteristics of OS/OSC inks.

Sample	Ink pH	*n*	*G′*-DSR$_{3/1}$	*G′*-DSR$_{5/3}$	*G″*-DSR$_{3/1}$	*G″*-DSR$_{5/3}$
OS-2	7.19±0.04^{a}	0.71±0.01^{e}	0.82±0.01^{c}	0.88±0.01^{de}	0.79±0.01^{c}	0.74±0.01^{d}
OS-1	7.18±0.05^{a}	0.73±0.01^{d}	0.82±0.01^{c}	0.87±0.01^{e}	0.77±0.01^{d}	0.72±0.01^{e}
OS-0.67	7.09±0.07^{b}	0.75±0.01^{c}	0.85±0.01^{b}	0.85±0.01^{f}	0.76±0.01^{d}	0.71±0.01^{ef}
OS-2-1%CS	6.45±0.04^{c}	0.77±0.01^{b}	0.95±0.01^{a}	0.97±0.01^{a}	0.89±0.01^{b}	0.94±0.01^{b}
OS-2-2%CS	6.42±0.04^{c}	0.82±0.01^{a}	0.95±0.01^{a}	0.98±0.01^{a}	0.99±0.01^{a}	0.99±0.01^{a}
OS-1-1%CS	6.44±0.05^{cd}	0.75±0.01^{cd}	0.82±0.01^{c}	0.90±0.01^{b}	0.79±0.01^{c}	0.84±0.01^{c}
OS-1-2%CS	6.35±0.04^{cd}	0.74±0.01^{cd}	0.80±0.01^{d}	0.89±0.01^{bc}	0.78±0.01^{d}	0.71±0.01^{ef}
OS-0.67-1%CS	6.36±0.04^{cd}	0.74±0.01^{cd}	0.80±0.01^{d}	0.90±0.01^{b}	0.77±0.01^{d}	0.70±0.01^{f}
OS-0.67-2%CS	6.33±0.05^{d}	0.73±0.01^{cd}	0.74±0.01^{e}	0.88±0.01^{cd}	0.73±0.01^{e}	0.68±0.01^{g}

Table S3. Thixotropic behavior (G') of OS/OSC inks

Sample	G'_1 (Pa)	G'_2 (Pa)	G'_3 (Pa)	G'_4 (Pa)	G'_5 (Pa)
OS-2	16.54±0.67^{i}	2.23±0.22^{e}	13.45±0.63^{i}	2.50±0.16^{f}	12.05±0.55^{i}
OS-1	19.81±0.65^{h}	2.20±0.19^{e}	16.28±0.72^{h}	1.85±0.22^{f}	14.19±0.51^{h}
OS-0.67	22.69±0.78^{g}	2.56±0.22^{e}	19.36±0.85^{g}	2.46±0.16^{f}	16.53±0.68^{g}
OS-2-1%CS	26.40±0.74^{f}	2.69±0.28^{e}	24.70±0.68^{f}	2.28±0.27^{f}	24.45±0.73^{f}
OS-2-2%CS	30.27±0.77^{e}	3.83±0.17^{d}	28.57±0.85^{e}	4.41±0.38^{d}	29.66±0.55^{d}
OS-1-1%CS	37.03±0.83^{d}	4.23±0.32^{d}	30.22±1.06^{d}	3.52±0.27^{e}	27.75±0.60^{e}
OS-1-2%CS	52.39±0.53^{c}	8.97±0.45^{a}	42.33±1.21^{c}	8.81±0.53^{a}	37.84±0.56^{c}
OS-0.67-1%CS	63.53±1.12^{b}	7.52±0.39^{b}	51.32±1.11^{a}	7.52±0.38^{b}	46.06±0.82^{a}
OS-0.67-2%CS	66.30±1.08^{a}	6.16±0.40^{c}	49.38±0.83^{b}	5.16±0.27^{c}	43.50±0.74^{b}

Table S4. Thixotropic behavior (G'') of OS/OSC inks

Sample	G''_1 (Pa)	G''_2 (Pa)	G''_3 (Pa)	G''_4 (Pa)	G''_5 (Pa)
OS-2	1.90±0.11^{f}	3.25±0.20^{g}	1.55±0.22^{e}	3.28±0.35^{d}	1.15±0.27^{d}
OS-1	2.25±0.12^{ef}	3.77±0.24^{fg}	1.76±0.21^{de}	3.45±0.32^{d}	1.28±0.28^{d}
OS-0.67	2.67±0.11^{e}	4.16±0.17^{f}	2.07±0.33^{de}	3.77±0.49^{d}	1.42±0.26^{d}
OS-2-1%CS	2.76±0.12^{e}	4.76±0.14^{e}	2.44±0.33^{d}	4.44±0.32^{d}	2.40±0.32^{c}
OS-2-2%CS	3.37±0.17^{d}	6.55±0.32^{d}	3.41±0.33^{c}	7.03±0.60^{c}	3.39±0.40^{b}
OS-1-1%CS	4.36±0.26^{c}	7.57±0.35^{c}	3.40±0.37^{c}	6.87±0.59^{c}	2.92±0.41^{bc}
OS-1-2%CS	5.82±0.38^{b}	12.45±0.33^{b}	4.54±0.44^{b}	12.16±0.55^{a}	3.18±0.41^{b}
OS-0.67-1%CS	6.22±0.33^{b}	12.24±0.51^{b}	4.85±0.49^{b}	10.84±0.70^{b}	3.43±0.28^{b}
OS-0.67-2%CS	8.66±0.46^{a}	13.09±0.49^{a}	6.26±0.38^{a}	12.32±0.51^{a}	4.26±0.38^{a}

Table S5. Rheological and printing characteristics of OS/OSC inks.

Sample	τ_y	τ_f	Layer
OS-2	5.29 ± 0.17^{f}	53.30 ± 0.70^{e}	5.28 ± 0.26^{e}
OS-1	5.41 ± 0.17^{ef}	53.98 ± 1.28^{de}	4.48 ± 0.34^{ef}
OS-0.67	5.55 ± 0.13^{ef}	55.58 ± 0.81^{d}	3.77 ± 0.22^{f}
OS-2-1%CS	5.61 ± 0.14^{ef}	49.30 ± 0.86^{f}	32.66 ± 0.32^{a}
OS-2-2%CS	5.80 ± 0.17^{e}	50.70 ± 0.85^{f}	33.26 ± 0.71^{a}
OS-1-1%CS	7.84 ± 0.16^{d}	55.67 ± 1.00^{d}	27.53 ± 0.67^{c}
OS-1-2%CS	8.34 ± 0.22^{c}	60.69 ± 0.85^{c}	28.90 ± 0.65^{b}
OS-0.67-1%CS	8.64 ± 0.12^{b}	62.56 ± 1.00^{b}	24.31 ± 0.86^{d}
OS-0.67-2%CS	9.61 ± 0.23^{a}	66.44 ± 1.08^{a}	24.52 ± 0.89^{d}

136 **Table S6.** Mechanical strength of POS/POSC hydrogels.

Sample	Tensile strength (g)			Ruptured distance (mm)			Compression modulus (kPa)		
	After printed	After 1 h	After 24 h	After printed	After 1 h	After 24 h	After printed	After 1 h	After 24 h
POS-2	1.25±0.26^{c}	0.89±0.15^{d}	0.09±0.11^{d}	2.28±0.38^{f}	1.43±0.32^{f}	0.60±0.22^{f}	1.22±0.11^{e}	0.85±0.12^{e}	0.31±0.04^{f}
POS-1	1.37±0.27^{c}	0.93±0.17^{d}	0.25±0.17^{d}	2.03±0.28^{f}	1.22±0.22^{f}	0.55±0.21^{f}	1.02±0.13^{e}	0.81±0.21^{e}	0.25±0.04^{f}
POS-0.67	1.62±0.27^{c}	0.97±0.16^{d}	0.29±0.16^{d}	1.47±0.38^{f}	1.02±0.22^{f}	0.52±0.22^{f}	0.76±0.11^{e}	0.34±0.08^{e}	0.12±0.06^{f}
POS-2-1%CS	8.33±0.32^{b}	11.18±0.95^{b}	9.28±0.27^{b}	15.26±0.51^{b}	19.43±0.73^{b}	14.22±0.43^{b}	10.38±0.80^{b}	16.51±0.66^{b}	8.77±0.53^{b}
POS-2-2%CS	8.44±0.32^{ab}	13.10±0.63^{a}	11.29±0.29^{a}	16.94±0.71^{a}	20.28±0.64^{a}	15.34±0.44^{a}	16.42±0.90^{a}	21.46±0.74^{a}	14.55±0.56^{a}
POS-1-1%CS	8.41±0.32^{ab}	6.53±0.67^{c}	2.59±0.31^{c}	11.32±0.56^{c}	8.42±0.54^{c}	4.48±0.44^{c}	8.50±0.68^{c}	7.52±0.68^{c}	3.44±0.43^{c}
POS-1-2%CS	8.61±0.28^{ab}	6.81±0.64^{c}	2.81±0.26^{c}	10.65±0.55^{c}	8.05±0.50^{c}	4.02±0.50^{cd}	7.58±0.67^{cd}	6.74±0.51^{c}	2.55±0.39^{d}
POS-0.67-1%CS	9.00±0.33^{ab}	7.11±0.72^{c}	2.61±0.33^{c}	8.54±0.34^{d}	6.73±0.49^{d}	3.51±0.38^{d}	6.52±0.69^{d}	5.17±0.33^{d}	1.97±0.39^{de}
POS-0.67-2%CS	9.13±0.26^{a}	7.25±0.68^{c}	2.84±0.23^{c}	7.58±0.44^{e}	5.50±0.34^{e}	2.56±0.40^{e}	6.62±0.73^{d}	4.50±0.37^{d}	1.47±0.43^{e}

137

Table S7. Water-holding characteristics of POS/POSC hydrogels.

Sample	T_{22} (ms)	T_{22} peak area (%)	Peak temperature (^{o}C)	ΔHr (J/g)
POS-2-1%CS	31.41±0.38^{b}	98.20±0.67^{a}	78.44±0.30^{b}	11.25±0.22^{b}
POS-2-2%CS	33.71±0.49^{a}	98.02±0.12^{ab}	79.63±0.51^{a}	12.94±0.35^{a}
POS-1-1%CS	23.83±0.38^{c}	97.36±0.18^{c}	75.73±0.57^{d}	11.09±0.33^{b}
POS-1-2%CS	20.70±0.56^{d}	97.53±0.13^{bc}	76.82±0.61^{c}	11.18±0.36^{b}
POS-0.67-1%CS	16.83±0.41^{e}	95.53±0.10^{d}	74.40±0.77^{e}	8.37±0.28^{c}
POS-0.67-2%CS	14.66±0.54^{f}	95.68±0.10^{d}	75.10±0.33^{de}	8.48±0.28^{c}

Table S8. Mass loss and decomposition of POS/POSC hydrogels.

Sample	Mass loss$_1$ (%)	Mass loss$_2$ (%)	Residual mass (%)	Decomposition (%/min)
POS-2	11.10±0.31^{b}	67.14±0.39^{b}	21.76±0.70^{d}	18.74±0.62^{a}
POS-1	11.37±0.27^{ab}	68.06±0.30^{b}	20.57±0.56^{d}	15.37±0.46^{b}
POS-0.67	11.94±0.28^{a}	69.55±0.33^{a}	18.51±0.61^{e}	14.77±0.49^{b}
POS-2-1%CS	9.92±0.43^{de}	64.95±0.42^{d}	25.12±0.85^{b}	10.52±0.47^{e}
POS-2-2%CS	9.43±0.39^{e}	63.84±0.70^{e}	26.72±1.13^{a}	10.23±0.43^{e}
POS-1-1%CS	10.37±0.38^{cd}	66.14±0.88^{c}	23.49±1.26^{c}	11.31±0.51^{de}
POS-1-2%CS	10.02±0.34^{de}	65.41±0.43^{cd}	24.56±0.77^{bc}	10.85±0.59^{de}
POS-0.67-1%CS	10.78±0.43^{bc}	67.42±0.45^{b}	21.80±0.87^{d}	12.48±0.55^{c}
POS-0.67-2%CS	11.38±0.39^{ab}	68.09±42^{b}	20.53±0.80^{d}	11.87±0.35^{cd}

142 **Table S9.** Thermal characteristics of POS/POSC hydrogels.

Sample	$\Delta Hr_{first\ peak}$ (J/g)	$\Delta Hr_{second\ peak}$ (J/g)	$\Delta Hr_{third\ peak}$ (J/g)	$\Delta Hr_{all\ peak}$ (J/g)	T_g (°C)	T_m (°C)
POS-2	63.65±1.00^{a}	28.94±0.82^{f}	-	92.60±1.81^{e}	93.51±1.05^{de}	239.61±0.84^{de}
POS-1	58.36±1.28^{b}	26.62±1.21^{f}	-	85.01±2.51^{f}	91.46±0.83^{ef}	238.53±0.58^{ef}
POS-0.67	53.29±1.33^{c}	17.34±1.57^{g}	-	70.63±2.89^{g}	89.45±1.17^{f}	236.63±1.06^{f}
POS-2-1%CS	50.79±1.06^{cd}	117.61±1.35^{c}	-	168.40±2.37^{c}	100.75±2.34^{b}	240.65±0.82^{cd}
POS-2-2%CS	51.46±1.37^{cd}	431.06±5.11^{a}	-	482.52±5.85^{a}	103.00±2.23^{a}	250.57±2.35^{a}
POS-1-1%CS	49.37±1.69^{d}	105.14±2.53^{d}	-	154.51±3.99^{d}	96.38±0.69^{c}	246.52±1.01^{b}
POS-1-2%CS	50.35±1.97^{cd}	357.07±5.10^{b}	-	407.42±6.96^{b}	95.36±0.69^{cd}	242.45±1.05^{c}
POS-0.67-1%CS	45.24±1.46^{e}	25.55±0.99^{f}	21.70±0.88^{b}	70.79±2.51^{g}	94.47±0.68^{cd}	242.46±1.06^{c}
POS-0.67-2%CS	48.68±1.05^{d}	47.68±1.00^{e}	33.34±1.28^{a}	96.37±2.03^{e}	92.13±0.76^{e}	241.27±0.87^{cd}

143

144 **Table S10.** Fitting R^2 of POSC hydrogels with different models.

Sample	pH 7.4					pH 5.0				
	Zero order	First order	Hixson-Crowell	Higuchi	Korsmeyer-Peppas	Zero order	First order	Hixson-Crowell	Higuchi	Korsmeyer-Peppas
POS-2-1%CS	0.7468	0.9810	-0.4309	0.9612	0.9992	0.7303	0.9766	-0.4258	0.9574	0.9869
POS-2-2%CS	0.6737	0.9734	-0.6267	0.9609	0.9979	0.7054	0.9714	-0.4946	0.9585	0.9874
POS-1-1%CS	-0.6154	0.9638	-3.1057	0.6497	0.9891	-0.2593	0.9536	-2.5140	0.7691	0.9863
POS-1-2%CS	-0.7392	0.9365	-3.2583	0.5842	0.9903	-0.2047	0.9539	-2.4181	0.7868	0.9890
POS-0.67-1%CS	0.1104	0.9370	-1.6945	0.8592	0.9895	-0.0090	0.9537	-2.0861	0.8662	0.9881
POS-0.67-2%CS	0.3383	0.9396	-1.2428	0.9116	0.9817	0.5127	0.9482	-0.9173	0.9451	0.9962

145

146 **Supporting Figure**

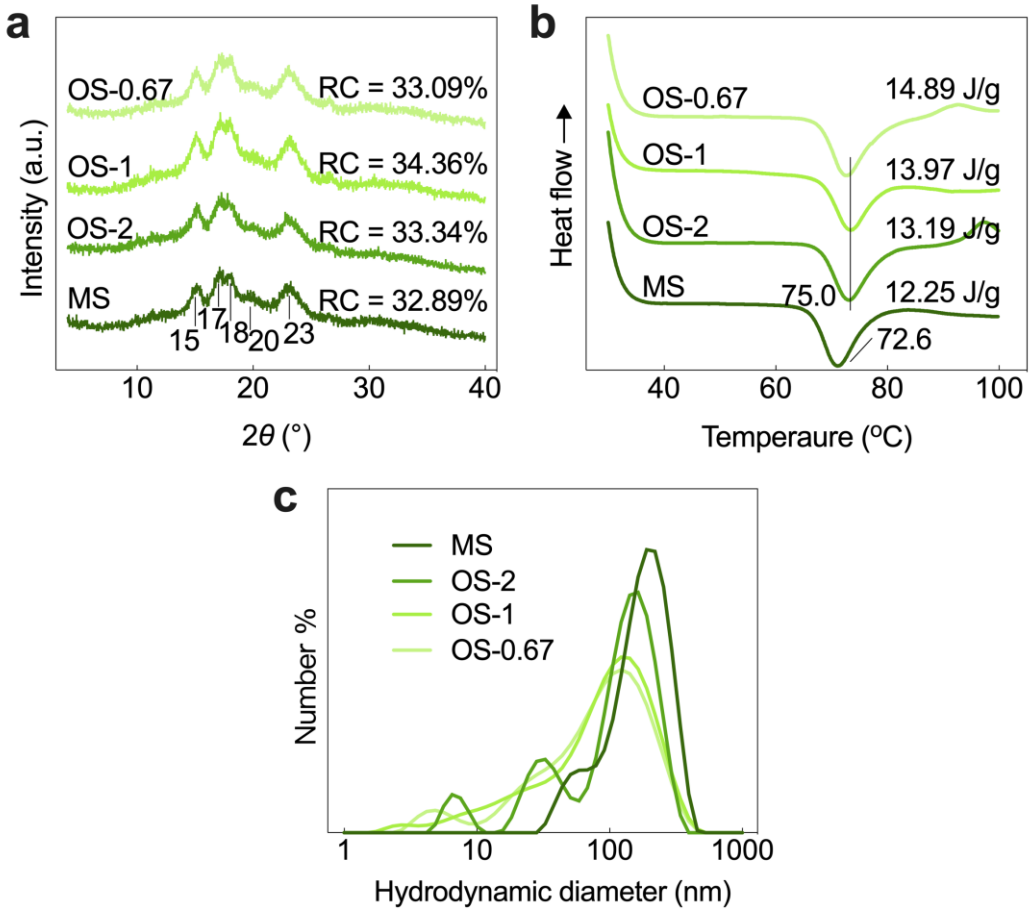

147

148 **Figure S1.** XRD curves (a), DSC curves (b), and hydrodynamic diameter distributions (c)

149 of MS/OS. (RC, relative crystallinity)

150

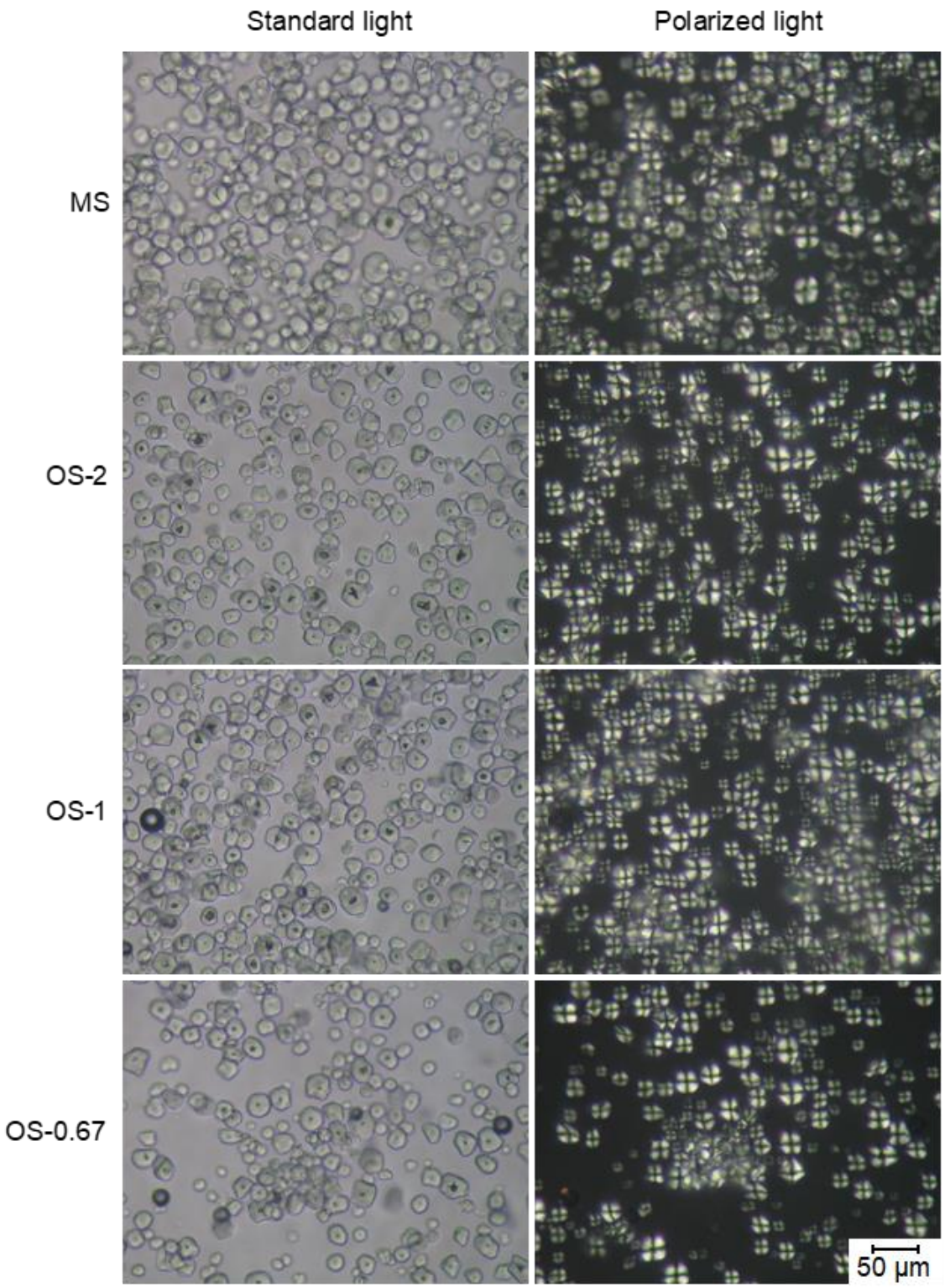

Figure S2. Morphology of MS/OS.

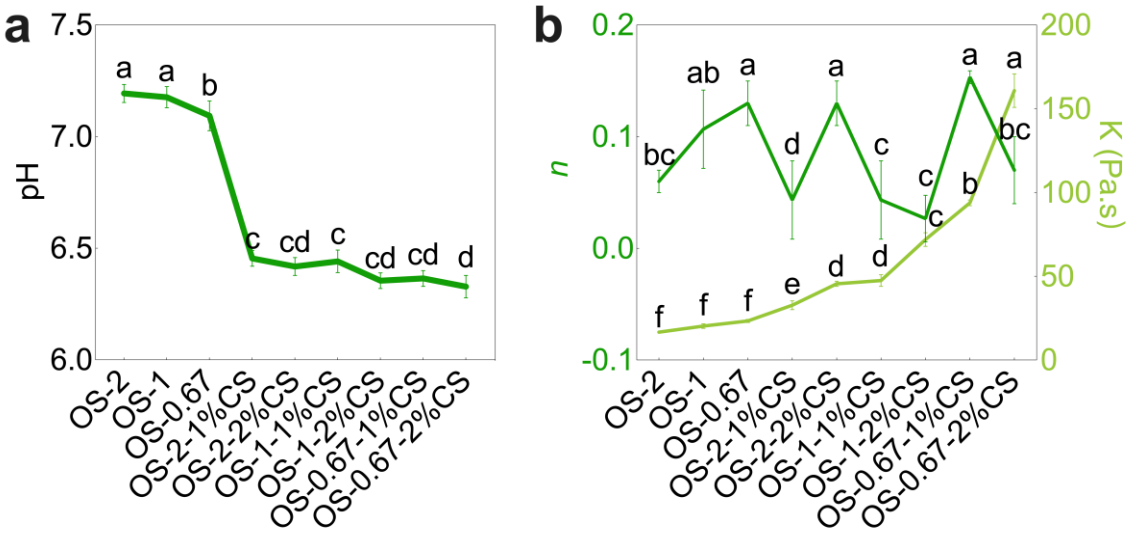

154

155 **Figure S3**. pH (a) and stabilizing shear (b) of OS/OSC inks.

156

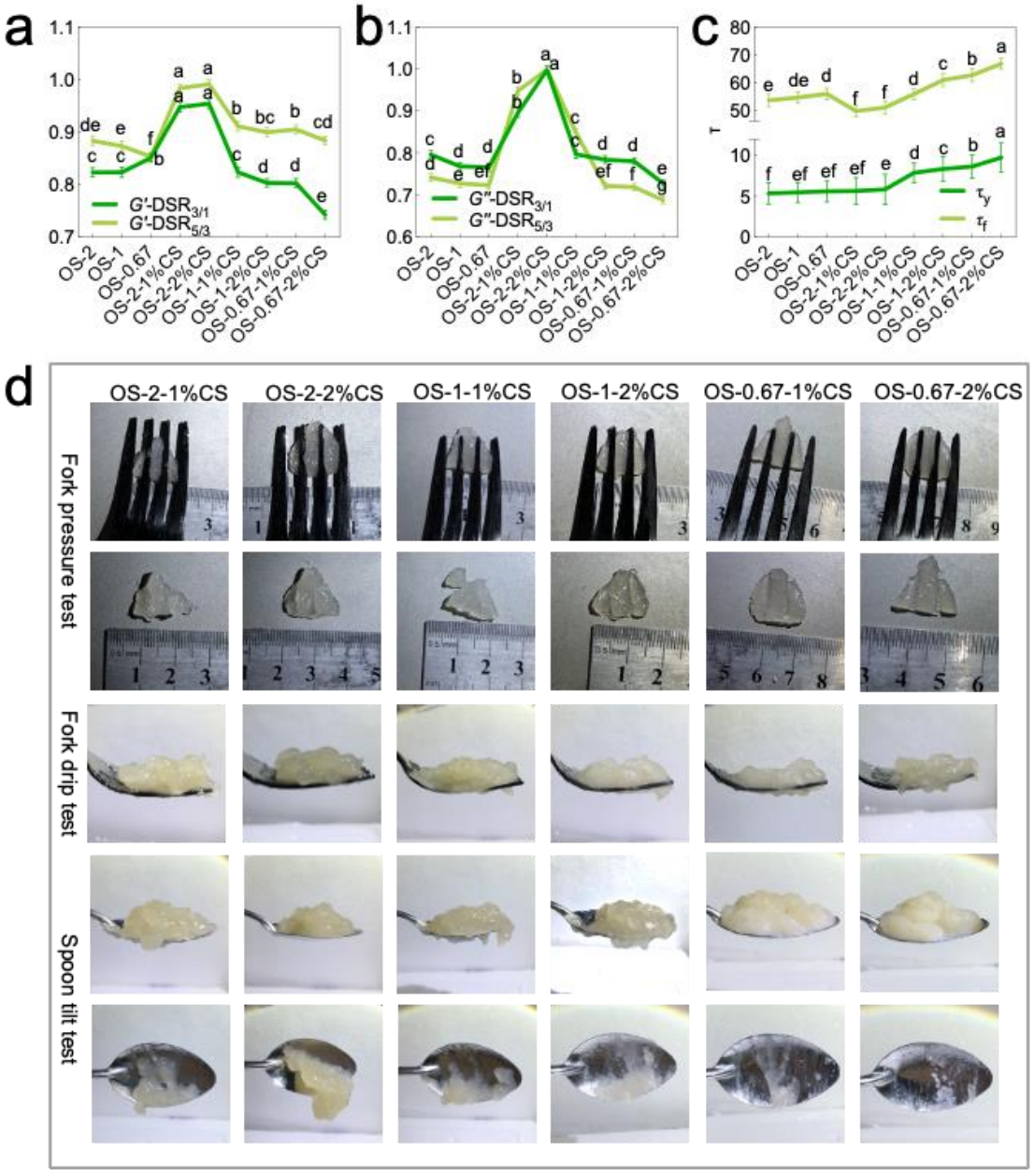

Figure S4. Thixotropy (a, b), strain shear (c), and fork and spoon test (d) of OSC inks.

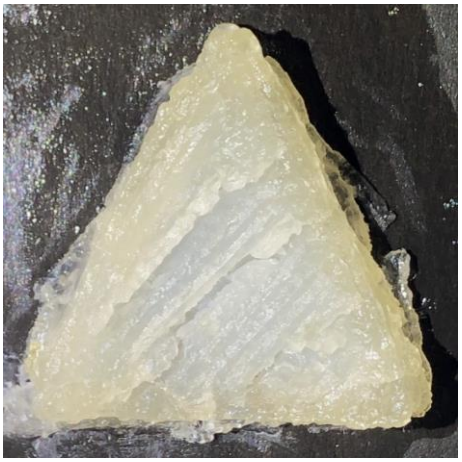

Figure S5. Section of POS-2-2%CS hydrogel after 7 days of placement.

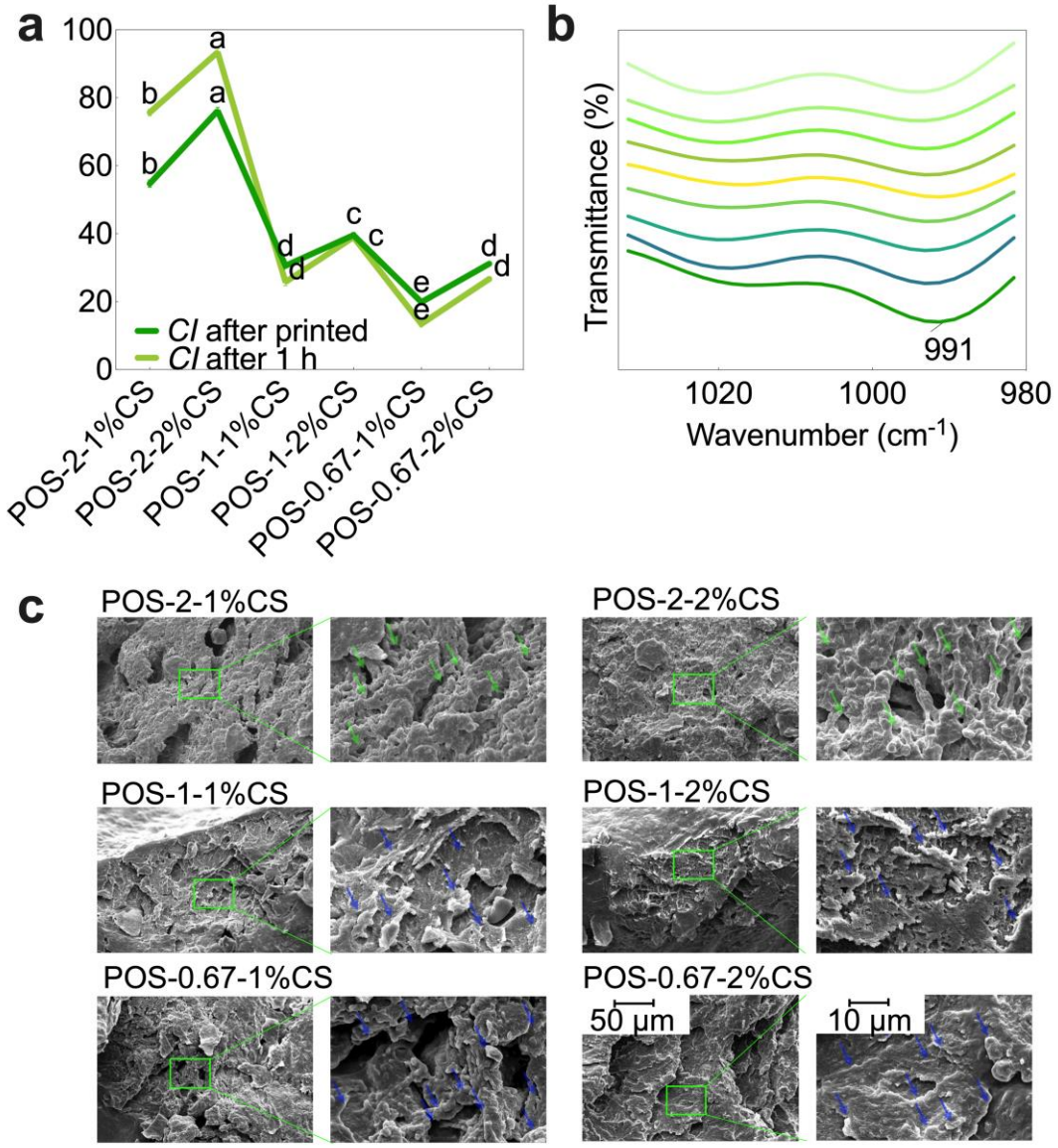

163

164 **Figure S6**. *CI* (a), two mediator spectra (b), and SEM images after 24 h storage (c) of

165 POS/POSC hydrogels.

166

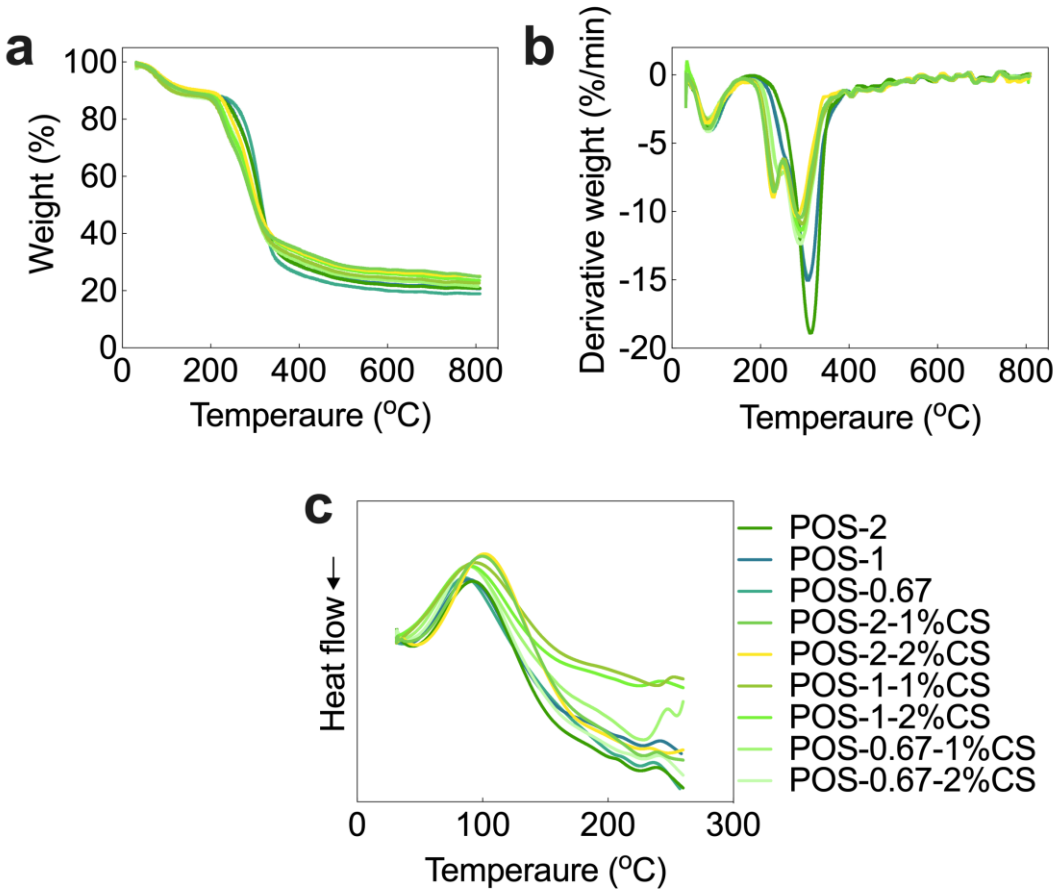

Figure S7. Thermal analysis (a, b, c) of POS/POSC hydrogels.

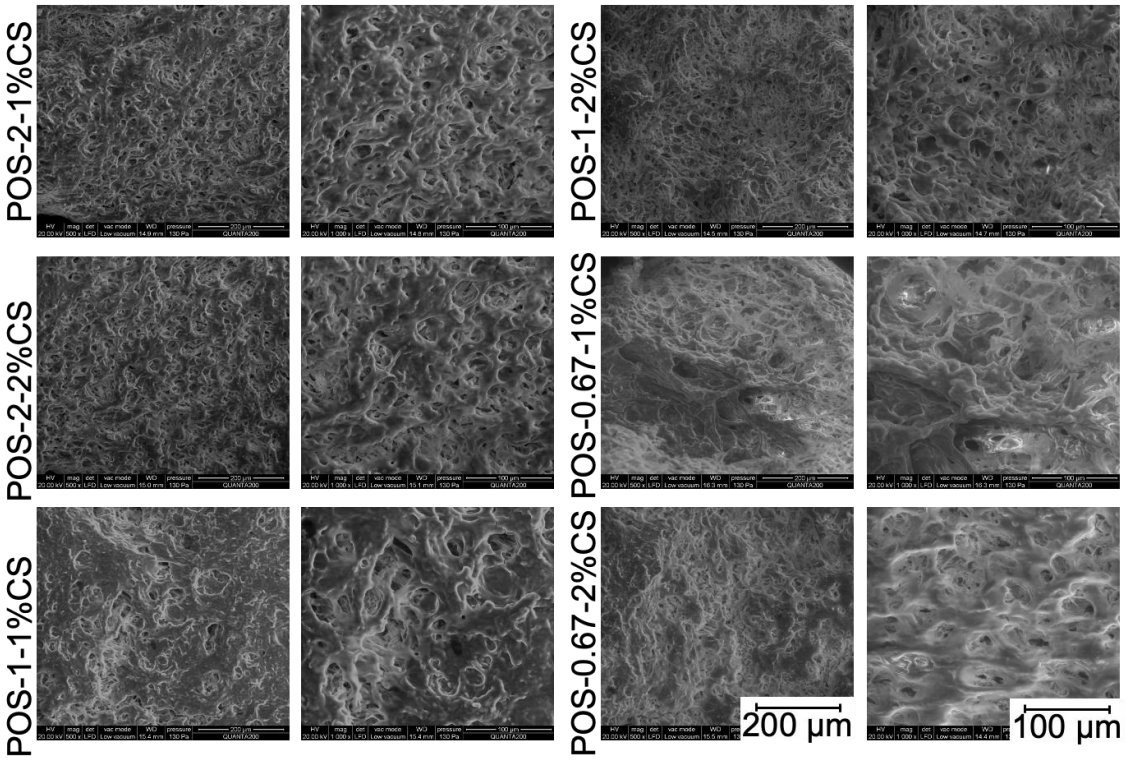

Figure S8. Environmental SEM images of POS/POSC hydrogels after swelling for 7 days.

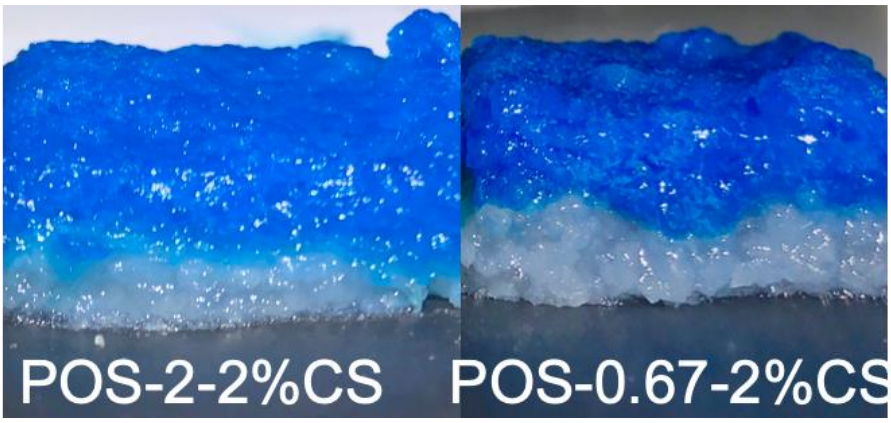

Figure S9. Self-healing performance of POSC hydrogels after 24 h.

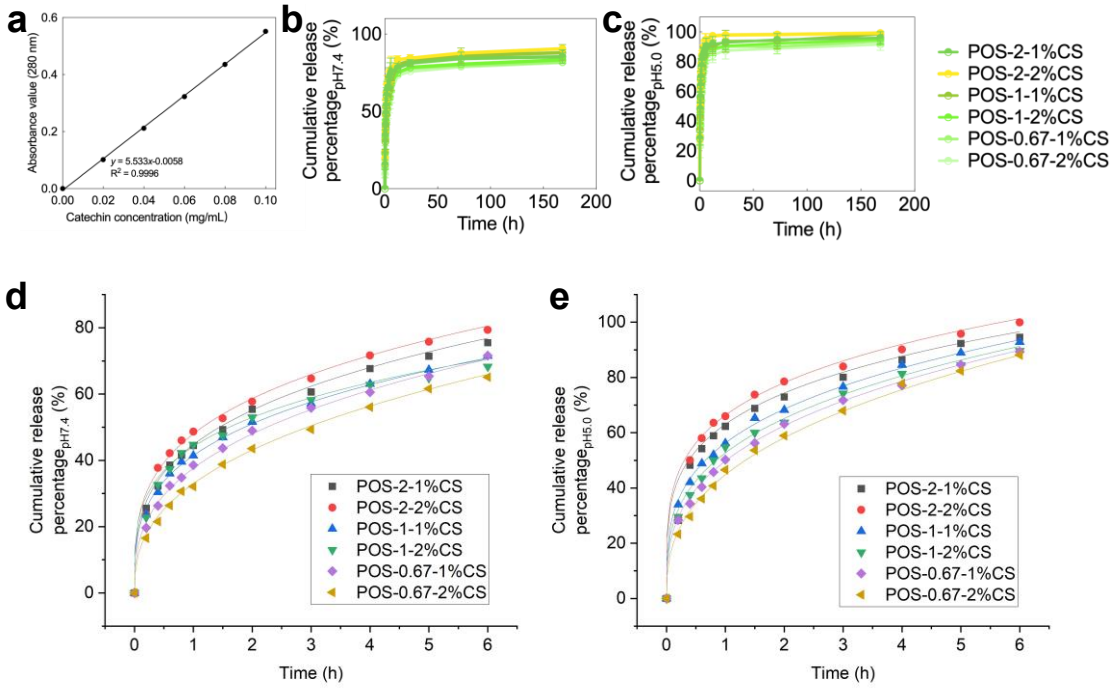

177

178 **Figure S10.** Calibration curve at 280 nm (a), release of 168 h (b, c), and fitted curve (d,

179 e) of catechin.

180

Supporting References

Chen, J., Li, X. X., Chen, L., & Xie, F. W. (2018). Starch film-coated microparticles for oral colon-specific drug delivery. *Carbohydrate Polymers,* 191, 242-254.

Chen, X., Yan, S., Wang, H., Hu, Z., Wang, X., & Huo, M. (2015). Aerobic oxidation of starch catalyzed by isopolyoxovanadate Na4Co (H2O) 6V10O28. *Carbohydrate Polymers,* 117, 673-680.

Khalfa, A. L., Becker, M. L., & Dove, A. P. (2021). Stereochemistry-Controlled Mechanical Properties and Degradation in 3D-Printable Photosets. *Journal of the American Chemical Society,* 143(42), 17510-17516.

Li, H., Tan, Y. J., Leong, K. F., & Li, L. (2017). 3D Bioprinting of Highly Thixotropic Alginate/Methylcellulose Hydrogel with Strong Interface Bonding. *ACS Applied Materials & Interfaces,* 9(23), 20086-20097.

Pematilleke, N., Kaur, M., Adhikari, B., & Torley, P. J. (2022). Instrumental method for International Dysphagia Diet Standardisation Initiative's (IDDSI) standard fork pressure test. *Journal of Food Engineering,* 326, 111040.

Tolvanen, P., Mäki-Arvela, P., Sorokin, A., Salmi, T., & Murzin, D. Y. (2009). Kinetics of starch oxidation using hydrogen peroxide as an environmentally friendly oxidant and an iron complex as a catalyst. *Chemical Engineering Journal,* 154(1-3), 52-59.

Wang, Y.-J., & Wang, L. (2003). Physicochemical properties of common and waxy corn starches oxidized by different levels of sodium hypochlorite. *Carbohydrate Polymers,* 52(3), 207-217.

Xue, L., Ma, Y., Yang, N., & Wei, H. (2021). Modification of corn starch via innovative contactless thermal effect from induced electric field. *Carbohydrate Polymers,* 255,

117378.